

WIYN Open Cluster Study. LXXVII. Radial-Velocity Measurements and Spectroscopic Binary Orbits in the Open Cluster NGC 7789

ANDREW C. NINE,¹ KATELYN E. MILLIMAN,^{2,1} ROBERT D. MATHIEU,¹
AARON M. GELLER,^{3,4} EMILY M. LEINER,^{3,1} IMANTS PLATAIS,⁵ AND
BENJAMIN M. TOFFLEMIRE^{6,1}

¹*Department of Astronomy, University of Wisconsin-Madison,
475 N Charter St, Madison, WI 53706, USA*

²*Department of Space Studies, American Public University,
111 W Congress St, Charles Town, WV 25414, USA*

³*Center for Interdisciplinary Exploration and Research in Astrophysics (CIERA)
and Department of Physics and Astronomy, Northwestern University,
1800 Sherman Ave., Evanston, IL 60208, USA*

⁴*Adler Planetarium, Department of Astronomy,
1300 S. Lake Shore Drive, Chicago, IL 60605, USA*

⁵*Department of Physics and Astronomy, Johns Hopkins University,
3400 N Charles St, Baltimore, MD 21218, USA*

⁶*Department of Astronomy, University of Texas at Austin,
2515 Speedway, Stop C1400, Austin, TX 78712, USA*

ABSTRACT

We introduce the stellar sample of the WIYN Open Cluster Study radial-velocity survey for the rich open cluster NGC 7789 (1.6 Gyr, [Fe/H] = +0.02). This sample lies within an 18' circular radius from the cluster center (10 pc in projection, or about 2 core radii), and includes giants, red-clump stars, blue stragglers, red stragglers, sub-subgiants, and main-sequence stars down to one mag below the turnoff. Our survey began in 2005 and comprises more than 9,000 radial-velocity measurements from the Hydra Multi-Object Spectrograph on the WIYN 3.5m telescope. We identify 564 likely cluster members and present the orbital solutions for 83 cluster binary stars with periods between 1.45 d and 4200 d. From the main-sequence binary solutions we fit a circularization period of $8.22^{+3.51}_{-1.35}$ d. We calculate an incompleteness-corrected main-sequence binary frequency of $31\% \pm 3\%$ for binaries with periods less than 10^4 days, similar to other WOCS open clusters of all ages. We detect a blue straggler binary frequency of $31\% \pm 15\%$, consistent with the similarly aged cluster NGC 6819.

1. INTRODUCTION

The WIYN Open Cluster Study (WOCS; Mathieu 2000) seeks to probe a wide variety of questions in stellar astrophysics by acquiring comprehensive photometric, astrometric, and spectroscopic data on a selected set of rich, nearby open clusters that span age and metallicity ($100 \text{ Myr} \lesssim t \lesssim 8 \text{ Gyr}$; $-0.4 \lesssim [\text{Fe}/\text{H}] \lesssim +0.3$). Within WOCS, extensive data have been combined and presented for M35 (150 Myr; Geller et al. 2010; Thompson et al. 2014; Leiner et al. 2015), NGC 6819 (2.5 Gyr; Platais et al. 2013; Yang et al. 2013; Milliman et al. 2014), M67 (4 Gyr; Geller et al. 2020, and references therein, in prep.), NGC 188 (7 Gyr; Sarajedini et al. 1999; Platais et al. 2003; Geller & Mathieu 2012) and NGC 6791 (8 Gyr; Platais et al. 2013; Tofflemire et al. 2014). These data have been the foundation for a wide array of scientific discoveries including insights into blue straggler (BSS) formation (Geller & Mathieu 2011; Milliman et al. 2015; Gosnell et al. 2015; Mathieu & Leiner 2019; Leiner et al. 2019), an age-rotation relationship for cool stars (Meibom et al. 2015), open cluster sub-subgiants (Milliman et al. 2016; Geller et al. 2017a,b; Leiner et al. 2017) and more (Sandquist et al. 2018; Deliyannis et al. 2019).

In this paper we introduce the stellar sample of the WOCS radial-velocity (RV) survey of NGC 7789 ($\alpha = 23^{\text{h}}57^{\text{m}}21^{\text{s}}.6$, $\delta = +56^{\circ}43'22''$ J2000). NGC 7789 is a well-populated, 1.6 Gyr (Gim et al. 1998b) open cluster at a distance of 2.0 kpc with $[\text{Fe}/\text{H}] = +0.02 \pm 0.04$ determined by Jacobson et al. (2011). Wu et al. (2009) measure a core radius of $8.82' \pm 0.91'$ and determine a cluster mass between $5150 M_{\odot}$ and $7710 M_{\odot}$ depending on the measurement method used.

Photometric studies of NGC 7789 begin with Burbidge & Sandage (1958) and include the *VI* photometry of Gim et al. (1998b) as well as the variability surveys of Jahn et al. (1995), Mochejska & Kaluzny (1999), and Zhang et al. (2003). A proper-motion study of McNamara & Solomon (1981) focused on evolved stars in NGC 7789. Here, we adopt the astrometry of *Gaia* Data Release 2 (*Gaia* DR2; Gaia Collaboration et al. 2016, 2018a,b). The use of *Gaia* DR2 allows for more detailed study of the cluster, including the confident identification of cluster members based on their proper motions and parallaxes (Cantat-Gaudin et al. 2018; Gao 2018).

The bright giants in NGC 7789 have also been the target of many spectroscopic abundance studies including Pancino et al. (2010), Jacobson et al. (2011), and Overbeek et al. (2015). These abundance studies as well as the RV surveys of cluster giants done by Gim et al. (1998a) and Casamiquela et al. (2016) have provided one to several RV measurements for most of the evolved stars in NGC 7789. With this paper we provide a complete RV time-series survey from the most luminous stars down to ~ 1 mag below the main-sequence turnoff. We also present the first comprehensive collection of spectroscopic binary orbit solutions for NGC 7789, and use these solutions for a first look at connections between binaries and the stellar population.

2. STELLAR SAMPLE AND PHOTOMETRY

The primary RV target sample for NGC 7789 that is the basis for this paper includes 1206 stars. The sample was initially built from the extensive VI CCD photometry of Gim et al. (1998b). This photometry was obtained from the Dominion Astrophysical Observatory 1.8 m Plaskett telescope and covers $\sim 18'$ radius from the center of NGC 7789. The full photometry set has over 15,000 stars, is complete from $V \sim 10$ to $V \sim 21$, and has a V standard error under ~ 0.01 mag down to our primary sample cutoff at $V = 15.0$. As in Milliman et al. (2014), we applied cuts in V and in $V - I$, such that $V < 15.0$ and that the stars above this cutoff had a measured $V - I$ in Gim et al. (1998b). We applied these criteria in order to select the upper main sequence, red clump, giant branch, and blue stragglers as well as other alternative stellar evolution products in the cluster.

We then cross-matched this sample of stars with *Gaia* DR2 using TOPCAT (Taylor 2005). From our sample of 1206 stars, we were able to retrieve matches for 1204 stars using a tolerance in position of $1''$. Of these, 1187 had full photometric and five-dimensional astrometric information. We use the proper motions to determine cluster memberships for our RV sample, discussed in detail in section 6.3. The remaining 17 stars had insufficient proper-motion information for complete membership determination (Section 6.4). Out of these 17 stars, 6 are RV members (Section 6.2), and are classified as cluster members. We adopt the photometry of *Gaia* DR2 for the remainder of this paper. As shown in Figure 1, our sample extends from $G \sim 10$ to $G \sim 15$, one mag below the main-sequence turnoff, and includes giant stars, a well-populated red clump, and a large number of BSS candidates.

3. WIYN OBSERVATIONS AND DATA REDUCTION

Our observations of NGC 7789 began in 2005 January using the Hydra Multi-Object Spectrograph (MOS; Barden et al. 1994) on the WIYN¹ 3.5m telescope. Our spectra are typically taken in a wavelength range of $\sim 500 \text{ \AA}$ centered on 5125 \AA , which encompasses the Mg B triplet and a rich array of narrow metal lines. We conduct our observations at 11th order, which yields a spectral resolution of $\sim 15,000$ - $20,000$ with a dispersion of 0.13 \AA/pix . More details on our observational setup can be found in Geller et al. (2008).

We follow the standard data acquisition and reduction procedures of the WOCS RV survey described in Geller et al. (2008). Briefly, for each configuration our data include one 100 s dome flat and two 300 s thorium-argon emission lamp spectra, one each before and after three science integrations. We use standard IRAF routines to bias subtract, dispersion correct, and extract each spectrum. We then flat-field, throughput correct, and subtract the sky from these spectra. In 2014 August we

¹ The WIYN 3.5m Observatory is a joint facility of the University of Wisconsin-Madison, Indiana University, and the National Optical Astronomy Observatory.

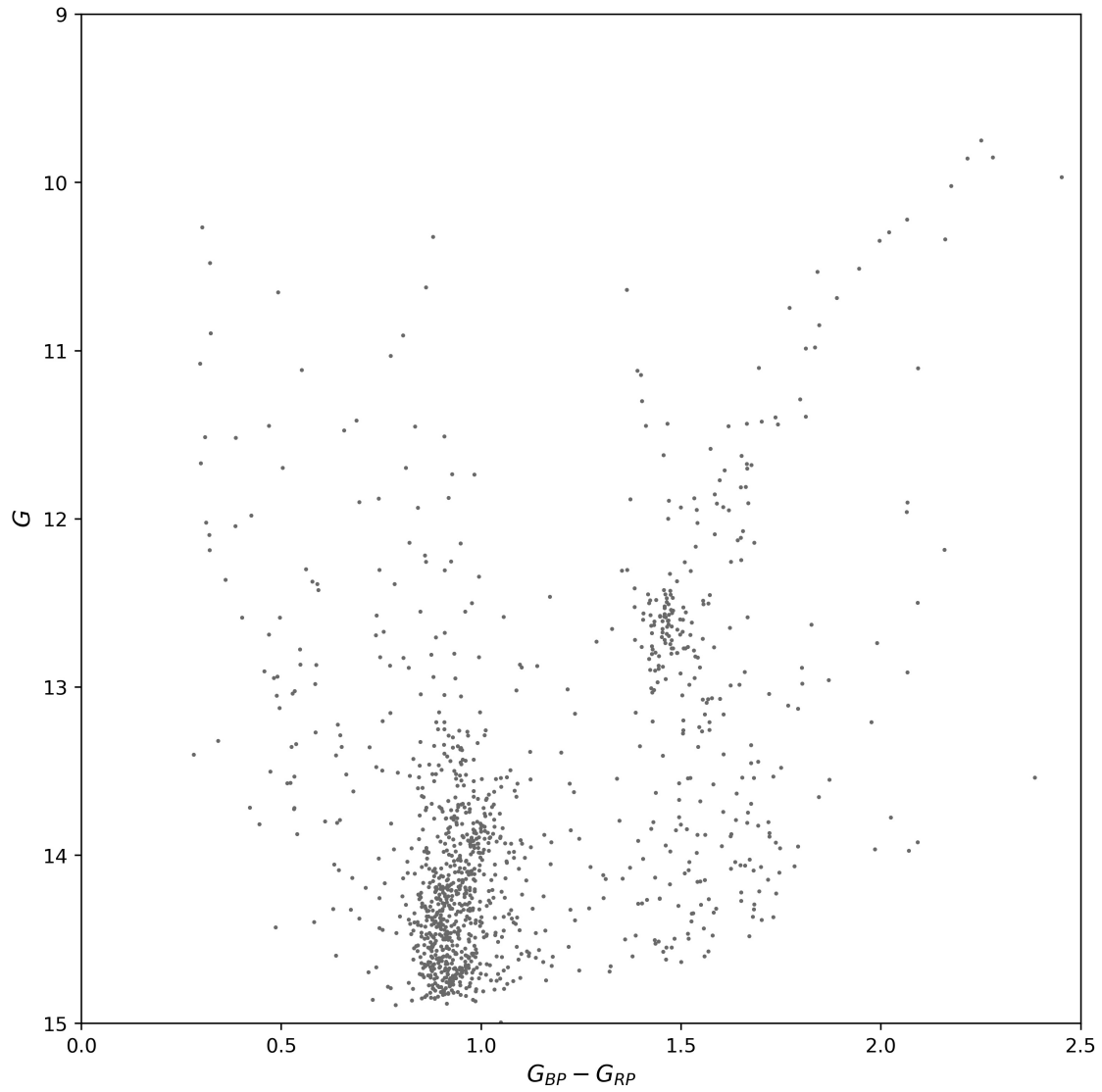


Figure 1. CMD of the NGC 7789 stars in our primary RV target sample based on the photometry of [Gaia Collaboration et al. \(2018b\)](#). The cluster’s giant branch, red clump, and upper main sequence are clearly present, as well as a large number of blue straggler candidates.

incorporated the L.A. Cosmic routine (van Dokkum 2001) for improved cosmic ray rejection.

The goal of this study is to conduct time-series observations of evolved stars, stars in the upper main sequence and stars on alternative evolutionary tracks in order to detect binaries and determine their orbital properties. For each observing run we use a prioritization system described in Geller et al. (2008) that emphasizes high-amplitude velocity-variable, short-period binaries, followed by longer period binaries. For a complete orbital solution, we typically require a minimum of 12 observations of sufficient quality as defined in Section 4, and that the best fit orbital solution has an rms residual velocity comparable to the velocity measurement errors. As of 2019 July, we have over 9,000 spectra spanning nearly 15 years for 1,198 stars in the primary sample. The resulting RV measurements and first results from these data are presented in this paper.

4. RV MEASUREMENT AND PRECISION

RVs for single narrow-lined stars (i.e., stars with $v \sin i < 10 \text{ km s}^{-1}$) are derived from the centroid of a one-dimensional cross-correlation function (CCF) with an observed solar template at zero velocity, converted to a heliocentric velocity, and corrected for the individual fiber offsets of the Hydra MOS. RVs for double-lined stars are derived following the two-dimensional cross-correlation technique TODCOR (Zucker & Mazeh 1994). Based on the analysis of Geller et al. (2008), we apply a quality threshold requirement of $\text{CCF} \geq 0.4$ for our RV measurements. We present all of our quality RV measurements for each star in Table 1, along with the Heliocentric Julian Date (HJD) of the observation and the height of the cross-correlation function. We also include the RV residual and the orbital phase of the observation for binary stars with completed orbital solutions.

Following the procedure of Geller et al. (2008) and Tofflemire et al. (2014) of fitting a χ^2 distribution to our observed distribution of RV standard deviations, we find our precision, σ_i , for the NGC 7789 narrow-lined stars to be $0.3 \pm 0.04 \text{ km s}^{-1}$ (Figure 2). This value is consistent with the value of $\sigma_i = 0.4 \text{ km s}^{-1}$ used in previous WOCS papers, which we adopt here as a conservative estimate.

For stars in our sample that are rapidly rotating ($v \sin i > 10 \text{ km s}^{-1}$), using an observed solar template results in a decrease in precision in our radial-velocity measurements due to their broadened CCFs. To achieve better RVs, we cross-correlate these stars against a grid of synthetic spectra² (Kurucz 1993; Meibom et al. 2009) with solar-metallicity, $\log g = 4.0$, $T_{\text{eff}} = 6500 \text{ K}$ (unless otherwise noted) and spanning a range of projected rotation velocities. We selected these particular values for temperature and $\log g$ based on the parameters near the turnoff of a 1.6 Gyr isochrone generated by the MESA Isochrones & Stellar Tracks (MIST; Dotter 2016

² The library is based on ATLAS9 (<http://kurucz.harvard.edu>) and the companion program SYNTHE used to compute the synthetic spectrum from the model atmosphere and line list.

Table 1. Radial-Velocity Measurements

ID	HJD-2,400,000 (days)	RV ₁ (km s ⁻¹)	Correlation Height ₁	O-C ₁ (km s ⁻¹)	RV ₂ (km s ⁻¹)	Correlation Height ₂	O-C ₂ (km s ⁻¹)	Phase
7003								
	53720.7009	-95.464	0.41	-1.64	-12.457	0.29	-2.26	0.132
	54275.9141	-76.535	0.67	-0.94	-28.382	0.56	1.64	0.261
	54676.9439	-58.680	0.85
	54683.9428	-39.360	0.77	-0.76	-69.085	0.72	1.18	0.583
	54715.7860	-36.947	0.67	-2.05	-74.254	0.62	0.04	0.622
	54723.8472	-25.573	0.78	-2.30	-86.237	0.65	0.70	0.886
	54724.7236	-26.386	0.76	2.20	-79.336	0.63	1.82	0.915
	54747.8150	-28.835	0.81	1.86	-82.320	0.67	-3.46	0.669
	54845.7016	-20.716	0.52	0.62	-91.026	0.34	-1.99	0.865
	55018.7892	-52.911	0.80

NOTE—Table 1 is published in its entirety in machine-readable format. A portion is shown here for guidance regarding its form and content.

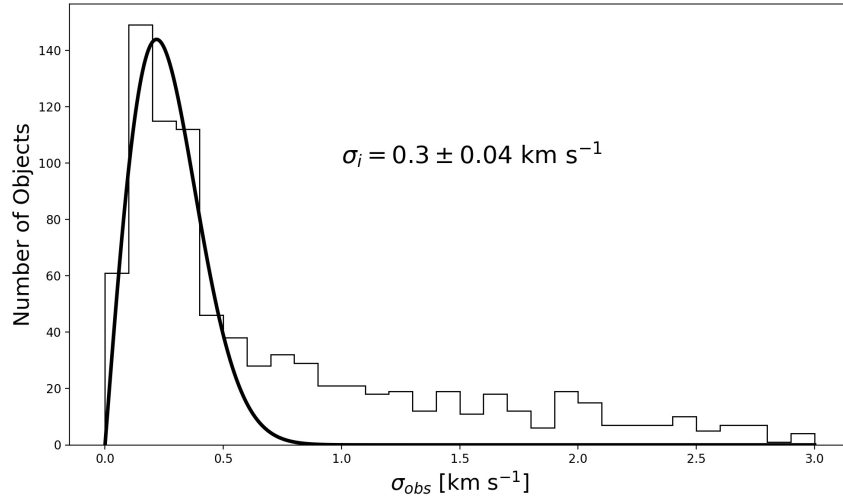


Figure 2. Histogram of the RV standard deviations from the first three observations of the narrow-lined stars in our primary sample. We overplot the best-fit χ^2 distribution function with a precision of 0.3 ± 0.04 km s⁻¹. The excesses above the theoretical distribution beginning at 0.5 km s⁻¹ are velocity-variable stars.

and references therein), corresponding to the CMD position of the majority of the rapidly rotating stars (Figure 3). Adjusting the temperature of the synthetic spectra improved the RVs only for the hottest of stars in our sample. We note these stars and their best-matched temperatures (the highest cross-correlation peak height) in Table 2. From the best-matched template we derive the RVs presented in Table 1 and note the $v \sin i$ of the synthetic spectra in Table 2.

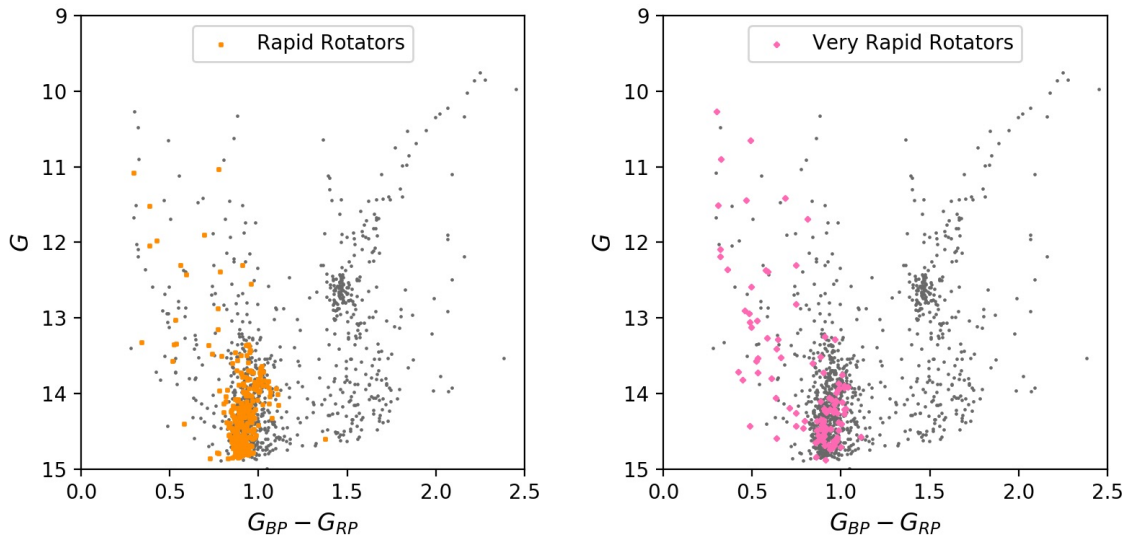


Figure 3. NGC 7789 CMD of the primary sample presented in this paper, constructed with *Gaia* DR2 photometry. Left panel: Rapid rotators with $10 \text{ km s}^{-1} < v \sin i < 120 \text{ km s}^{-1}$ are shown by orange squares. Right panel: Very rapid rotators with $v \sin i > 120 \text{ km s}^{-1}$, for which we cannot derive accurate RVs, are shown with pink diamonds.

We assign a precision to these rapid rotators (RR) using the following relationship from Geller et al. (2010):

$$\sigma_i = 0.38 + 0.012(v \sin i). \quad (1)$$

The above procedure does not work consistently for stars with $v \sin i$ greater than $\sim 120 \text{ km s}^{-1}$ because of their very broad CCFs. We label stars in our sample that are rotating faster than this as very rapid rotators (VRR), and we are unable to get accurate RV measurements or membership information for these stars.

In our sample, we identified 273 RR and 113 VRR stars. We plot the CMD location of 270 of the RR stars and all 113 VRR stars in Figure 3. As expected, most of these stars are hot and blue, with $G_{BP} - G_{RP} \leq 1.0$, and are concentrated on the upper main sequence (MS). These stars represent approximately 50% of the main-sequence stars in our primary sample.

5. COMPLETENESS

The primary target sample in this paper is comprised of 1206 stars with RV measurements starting in 2005. For our survey we constantly reevaluate the observing priority of each star. Generally we classify stars as single or velocity variable after three observations (Mathieu 1983; Geller & Mathieu 2012), and we then prioritize velocity-variable stars for continued observations until we determine an orbital solution. When we identify a VRR we move it to the bottom of our observation priority because we are unable to derive accurate RVs for such rapid rotators.

The percentages of stars for which we have three or more observations (excluding VRRs) as a function of cluster radius and of G magnitude are shown in Figure 4. We are able to classify almost 99% of stars in our primary stellar sample of NGC 7789 as single (by which we mean non-velocity variable), velocity-variable, or as VRRs. There are no significant biases in the classified stars with radius or magnitude.

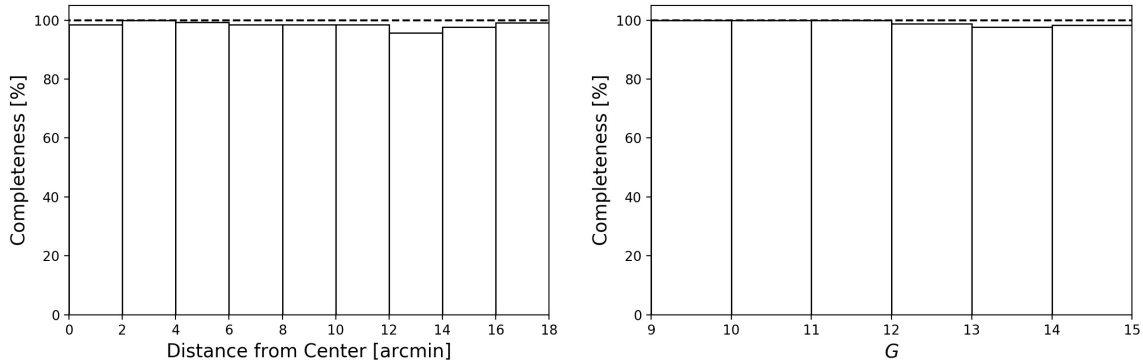


Figure 4. Percentage of stars in our sample (excluding VRRs) that have three or more RV observations with respect to distance from the cluster center (left) and G magnitude (right).

6. RESULTS OF RV STUDY

6.1. *Velocity-Variable Stars*

We define velocity-variable stars as having RV standard deviations (the external error, e) greater than 4 times the precision (the internal error σ_i , or i , described in Section 4)³, that is $e/i > 4$ (Geller et al. 2008). For each star with three or more observations we calculate the \overline{RV} and e/i , and classify it as single or velocity variable. Based on a Monte Carlo analysis for the NGC 7789 RV measurements, this procedure identifies 84% of all binaries under 1,000 days and 60% of all binaries with periods under 10,000 days (Section 8).

We present the coordinates, *Gaia* DR2 photometry, number of observations, \overline{RV} , \overline{RV} standard error, e/i , proper-motion membership probability (P_μ ; Section 6.3), RV membership probability (P_{RV}), and membership classification for all of the stars we have observed in NGC 7789 as of 2019 July in Table 2. For each binary star with a completed orbital solution, the center-of-mass velocity, γ , its error, and whether it is a single- or double-lined binary are also included in Table 2.

³ For consistency with previous WOCS papers and to prevent confusion with other uses of σ in this paper, we will use i to indicate internal precision for the rest of the paper.

Table 2. Radial-Velocity Summary Table

ID	α (J2000)	δ (J2000)	G	$G_{BP} - G_{RP}$	N	\bar{RV} (km s^{-1})	Std. Err. (km s^{-1})	e/i	P_μ (%)	P_{RV} (%)	Class	γ_{RV} (km s^{-1})	γ_{RVe} (km s^{-1})	Comment
1001	23 57 24.11	56 43 38.8	13.93	0.95	19	-49.54	0.87	0.55	87	39	SNM	RR (100 km s^{-1})
1002	23 57 18.72	56 43 50.8	13.73	0.94	3	-36.48	0.22	0.55	0	0	SNM
1003	23 57 29.55	56 42 23.5	12.33	1.47	3	-53.89	0.27	0.67	100	95	SM
1004	23 57 10.40	56 42 49.4	9.86	2.22	5	-53.58	0.2	0.51	99	95	SM
1005	23 57 31.85	56 41 22.1	11.1	1.69	3	-56.06	0.27	0.67	...	84	SM
1006	23 57 10.06	56 40 56.7	10.74	1.77	16	-53.08	2.09	5.24	89	93	BM	-54.963	0.183	SB1
1007	23 57 34.30	56 46 2.9	11.69	0.5	3	-4.05	0.1	0.26	0	0	SNM
1008	23 57 3.25	56 45 58.0	9.75	2.25	3	-53.46	0.08	0.19	100	95	SM
1009	23 57 52.04	56 42 25.6	10.29	2.02	3	-52.46	0.17	0.43	0	94	SNM
1010	23 57 43.94	56 39 42.8	11.51	0.31	11	18.93	3.79	9.48	...	0	VRR	VRR

NOTE—Table 2 is published in its entirety in machine-readable format. A portion is shown here for guidance regarding its form and content.

Table 3. Gaussian Fit Parameters for Cluster and Field RV Distributions

Parameter	Cluster	Field
Ampl. [number]	82.5 ± 3.3	5.7 ± 0.8
\overline{RV} [km s ⁻¹]	-53.5 ± 0.1	-36.7 ± 4.5
σ [km s ⁻¹]	1.5 ± 0.1	25.7 ± 4.7

6.2. RV Membership Probabilities

We follow the standard WOCS procedure and calculate the RV membership probability of a given star, P_{RV} in Table 2 using the equation:

$$P_{RV}(v) = \frac{F_{cluster}(v)}{F_{field}(v) + F_{cluster}(v)}. \quad (2)$$

$F_{cluster}$ and F_{field} are Gaussian functions simultaneously fit to the cluster and field-star populations using our sample of all single stars with three or more RV measurements. We plot these RVs and Gaussian functions in Figure 5 and record the parameters for these Gaussian fits in Table 3.

The RV survey of giant stars by Gim et al. (1998a) found an average RV of -54.9 ± 0.9 km s⁻¹ (s.d.) based on 50 stars and the abundance study of Jacobson et al. (2011) found an average RV of -54.7 ± 1.3 km s⁻¹ based on 26 evolved stars in NGC 7789. Overbeek et al. (2015) found an average RV of -54.6 ± 1.0 km s⁻¹ based on their study of 32 evolved stars. Our Gaussian fit to the cluster distribution is consistent with these studies, with a measured \overline{RV} of -53.5 ± 1.5 km s⁻¹. Our result also matches that of Casamiquela et al. (2016) who found a median RV of -53.6 ± 0.6 km s⁻¹ for seven red clump stars in NGC 7789. Geller et al. (2008) and Geller et al. (2015) found that the WOCS RV system is on the same zero-point as the DAO (Fletcher et al. 1982) and CfA (Latham et al. 1985) systems.

We note a clear separation between the cluster and field populations based on P_{RV} (Figure 6) and we adopt the standard WOCS membership threshold of $P_{RV} \geq 50\%$ for NGC 7789. We estimate from the cluster and field Gaussian functions a field star contamination of 5% at this membership threshold.

6.3. Proper-Motion and Radial-Velocity Memberships

We compare our RV membership results to the astrometric data retrieved from *Gaia* DR2. We were able to obtain complete astrometric information for 1187 stars in our primary sample. For each of the sources returned, we check the associated astrometric excess noise (ϵ_i) and the significance of the excess noise (D), which determine the disagreement between the observations of a source and the best-fitting astrometric model. For our derivation of P_μ for this cluster, we reject those sources which have $\epsilon_i \geq 10^{-3}$, which corresponds to $D \gtrsim 10^{-2}$. By rejecting these sources we aim to

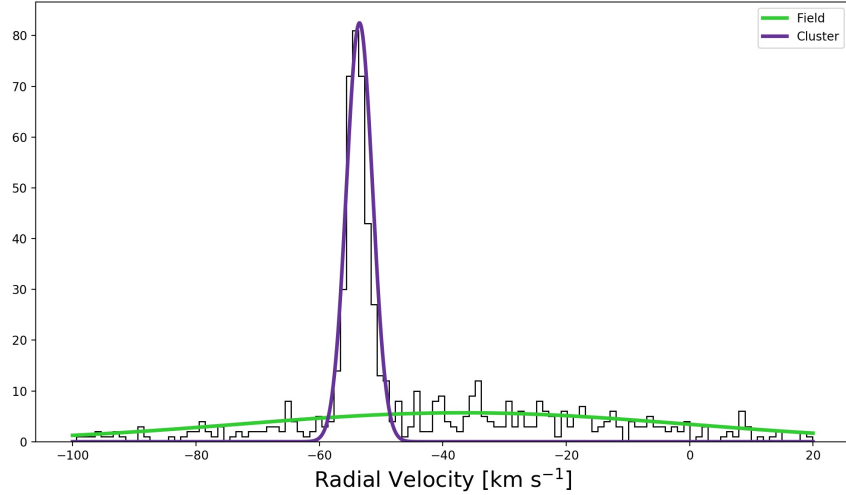


Figure 5. Histogram of the RV distribution of single stars, $e/i < 4$, with three or more RV observations. Also plotted are the Gaussian distributions fit to the cluster (the large peak at a mean velocity of -53.5 km s^{-1} ; purple line), and the field (green line).

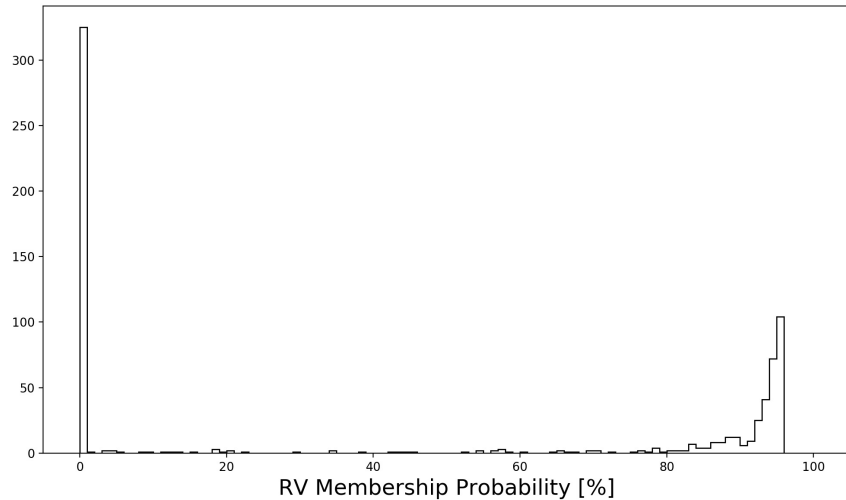


Figure 6. Histogram distribution of the radial-velocity membership probabilities of single stars (those with $e/i < 4$) in NGC 7789.

minimize the effects of any systematic variations in the astrometric data. We rejected a total of 85 stars from our sample, leaving 1102 stars with complete and low-noise astrometry as determined by *Gaia* DR2.

We use the astrometry from these 1102 stars to construct a two-dimensional Gaussian fit in proper-motion space in a similar manner as with the RVs. In this case, we fit two-dimensional Gaussian functions simultaneously to the proper motions of both cluster member and field stars. A more general description of this process is laid out in [Gao \(2018\)](#). We show the two-dimensional histogram of the proper motions

Table 4. Two-Dimensional Gaussian Fit Parameters for Cluster and Field Proper Motions

Parameter	Cluster	Field
Ampl. [number]	57.0 ± 1.3	0.2 ± 0.1
$\overline{\mu_{\alpha*}}$ [mas yr ⁻¹]	-0.959 ± 0.003	-1.8 ± 1.0
$\overline{\mu_{\delta}}$ [mas yr ⁻¹]	-1.986 ± 0.003	-1.6 ± 0.9
$\sigma_{\alpha*}$ [mas yr ⁻¹]	0.131 ± 0.003	1.5 ± 2.0
σ_{δ} [mas yr ⁻¹]	0.140 ± 0.004	1.9 ± 2.5

obtained from *Gaia* DR2 in Figure 7, and the Gaussian fits are shown in Figure 8. We also show the parameters for these fits in Table 4.

As with the RVs, there is a clear separation in P_{μ} between cluster and field populations, as shown in Figure 9. We again adopt the WOCS standard membership threshold of $P_{\mu} \geq 50\%$. We estimate from the amplitudes of the one-dimensional Gaussian functions fit to the cluster and field populations a field-star contamination of $\sim 4\%$ at this threshold.

Where available we list the P_{μ} in Table 2. In Figure 10 we plot the membership percentages from our RV study and *Gaia* DR2 proper motions. We find the majority of stars that overlap between the data sets have membership classifications that agree. As noted above, we expect a field star contamination of 5% within our sample of stars with $P_{RV} \geq 50\%$ based on the Gaussian fits to the cluster and field star distribution. Comparing the P_{μ} and P_{RV} values we indeed find $\sim 7\%$ of the stars with $P_{RV} \geq 50\%$ have proper motions that identify them as field stars, as can be seen in Figure 10.

We note that in Figure 10 there also appear a substantial number of stars for which $P_{RV} < 50\%$ and $P_{\mu} > 50\%$. Most of these stars are highly velocity variable, such that their mean RVs do not coincide with the mean RV of the cluster, but do include the mean within the range of their minimum and maximum measured RVs. There are 29 stars, however, that are either not velocity variable, rapidly rotating, or whose velocity variability does not include the mean RV of the cluster. Under the conservative assumption that these stars are all cluster nonmembers, they comprise $\sim 3\%$ of our sample, consistent with our estimate.

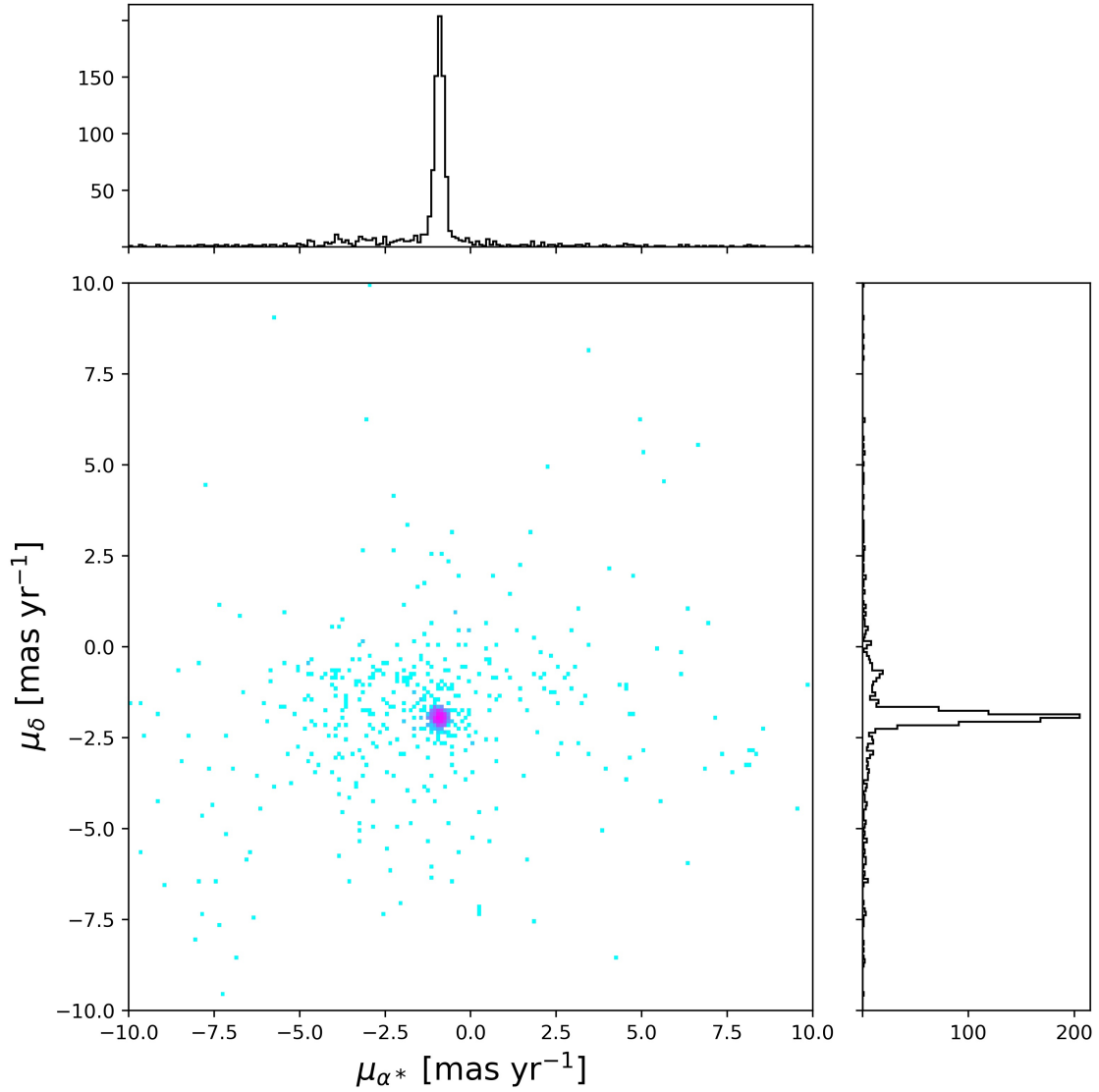


Figure 7. Two-dimensional histogram showing the *Gaia* DR2 proper motions of the stars in our primary sample in both right ascension and declination. On each axis we also plot the corresponding one-dimensional histogram in each direction. Cluster member stars appear as a clear overdensity in each plot.

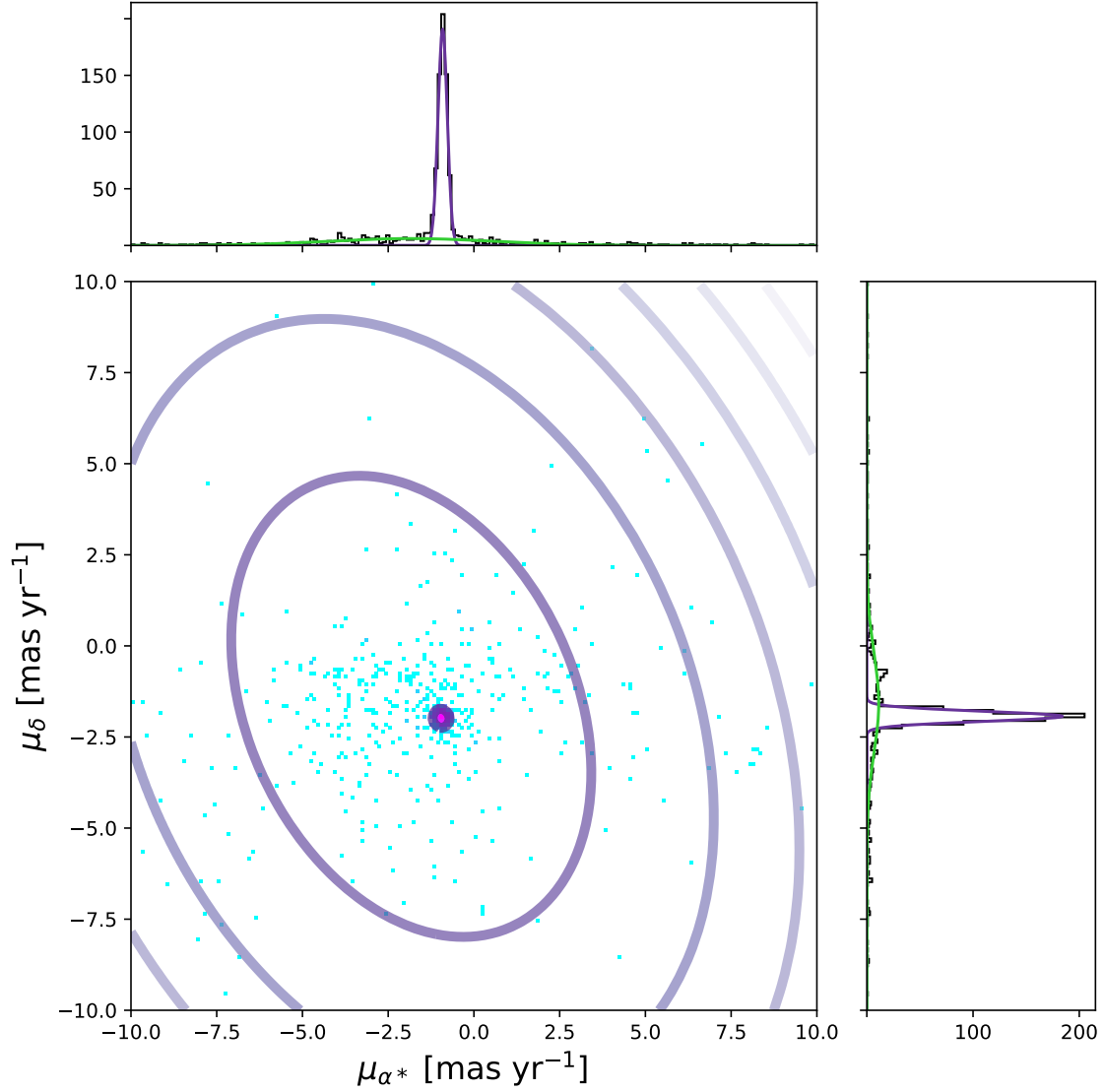


Figure 8. As in Figure 7, with the corresponding Gaussian fits overplotted. The fit to the cluster is tightly concentrated around the cluster proper motions in both the one-dimensional and two-dimensional cases, while the fit to the field is much more dispersed in proper-motion space. The contours in the central figure trace the N-sigma confidence intervals for both of the fits; the confidence intervals to the cluster are very tightly concentrated.

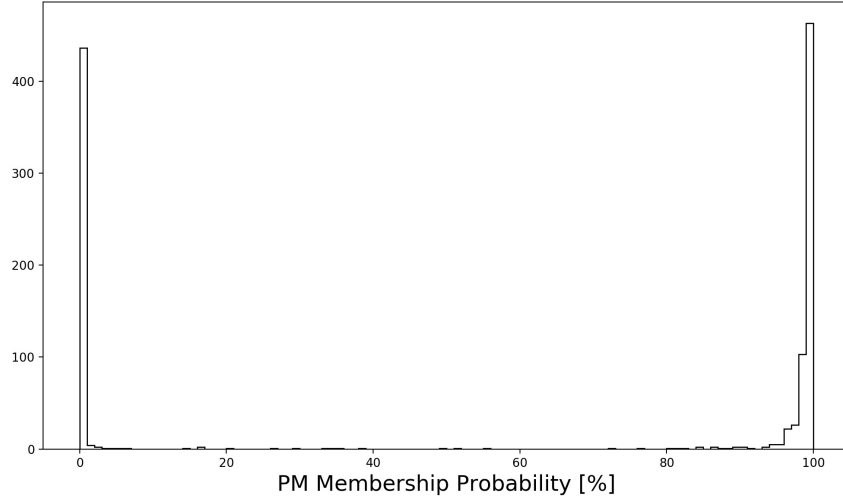


Figure 9. Histogram of the distribution of proper-motion membership probabilities for the stars with complete and low-noise astrometric data from *Gaia* DR2.

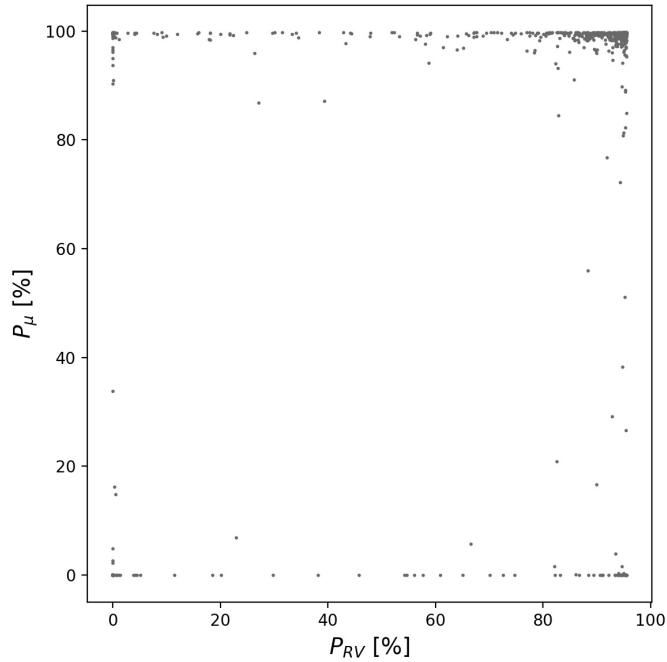


Figure 10. Our radial-velocity membership probabilities compared with our proper-motion membership probabilities derived from *Gaia* DR2 for the stars in our sample that have been observed at least three times and have complete and low-noise astrometry available, excluding VRRs ($n = 979$).

6.4. Membership Classification of Stars

Following previous WOCS procedure (Geller et al. 2015), we give in Table 2 membership classifications for stars in NGC 7789. The classifications are defined below

Table 5. Number of Stars Within Each Classification

Classification	N Stars
SM	459
SNM	436
BM	83
BNM	30
BLM	22
BLN	32
BU	8
VRR	113

for ease of reference here. Table 5 lists the number of stars in each membership classification.

Single Member (SM): Stars that have $e/i < 4$, $P_{RV} \geq 50\%$, and $P_\mu \geq 50\%$.

Single Non-member (SNM): Stars that have $e/i < 4$ and either $P_{RV} < 50\%$ or $P_\mu < 50\%$.

Binary Member (BM): Velocity-variable stars that have a completed orbital solution, $P_{RV} \geq 50\%$, and $P_\mu \geq 50\%$.

Binary Non-member (BNM): Velocity-variable stars that have a completed orbital solution and either $P_{RV} < 50\%$ or $P_\mu < 50\%$.

Binary Likely Member (BLM): Velocity-variable stars that do not have a completed orbital solution, $P_{RV} \geq 50\%$, and $P_\mu \geq 50\%$.

Binary Likely Non-member (BLN): Velocity-variable stars that do not have a completed orbital solution. Either P_{RV} or P_μ is $< 50\%$ and the range of RVs does not include the cluster mean, making it unlikely that the orbital solution will place the star within the cluster distribution.

Binary Unknown (BU): Velocity-variable stars that do not have a completed orbital solution. P_{RV} is $< 50\%$, but P_μ is $\geq 50\%$, and the range of individual RVs includes the cluster mean, making it possible that the binary could be a member.

Very Rapid Rotator (VRR): Stars that are too rapidly rotating ($v \sin i > 120 \text{ km s}^{-1}$) for accurate RV measurements.

For those 85 stars discussed in Section 6.3 and the 6 discussed in Section 2 which do not have PM information available, we assign membership based solely on their RV information, using similar criteria as listed above.

6.5. Color-Magnitude Diagram

Using the *Gaia* DR2 photometry and our three-dimensional membership information we present a cleaned CMD of NGC 7789 members in Figure 11. This CMD includes all three-dimensional BM, BLM, and SM stars. The cleaned CMD clearly shows the main sequence, crowded with velocity-variable stars, a very well-defined

red giant branch (RGB), and a populous red clump at $G \sim 13$. A number of BSS remain, which we discuss in more detail in Section 11.

We also show a 1.6 Gyr MIST (Dotter 2016) isochrone with a distance of 1.8 kpc, $A_V = 0.85$, and $[\text{Fe}/\text{H}] = 0.023$. These figures are roughly consistent with the heliocentric distance of 2074.7 ± 4.4 pc as measured by Cantat-Gaudin et al. 2018, $E(B - V) = 0.28 \pm 0.02$ as measured by Wu et al. (2007), and $[\text{Fe}/\text{H}] = 0.02 \pm 0.04$ as measured by Jacobson et al. (2011). The parameters used in our isochrone fitting are not meant to supersede those already published. Our isochrone is meant rather to guide the eye and serve as a reference point to distinguish between MS stars and BSS candidates.

6.6. Sub-Subgiants and Red Stragglers

We note two three-dimensional-member stars are sub-subgiant (SSG) candidates that fall significantly to the red and fainter than the subgiant branch and RGB with $G_{BP} - G_{RP} \sim 1.2$ to 1.4. (Additional background on SSGs can be found in Geller et al. 2017a.) The candidates are WOCS 20035 and WOCS 35033. WOCS 20035 has $G_{BP} - G_{RP} = 1.18$, $P_{RV} = 95\%$, and $P_\mu = 99\%$. WOCS 35033 in turn has $G_{BP} - G_{RP} = 1.38$, $P_{RV} = 94\%$, and $P_\mu = 93\%$. WOCS 20035 is velocity variable with a relatively low amplitude of ~ 7 km s⁻¹, but does not yet have a complete orbital solution. WOCS 35033 is a rapid rotator with a best-fit $v \sin i$ of 120 km s⁻¹; at the consequent poorer measurement precision of ~ 2 km s⁻¹, we have not detected velocity variability (see Equation 1). They are both targets of ongoing study.

We also note two three-dimensional member stars that lie to the red of the RGB: WOCS 19016 ($G = 13.7$, $G_{BP} - G_{RP} = 1.68$) and WOCS 22023 ($G = 14.2$, $G_{BP} - G_{RP} = 1.47$). These stars lie in the region of the CMD consistent with red stragglers (RSS; more background also can be found in Geller et al. 2017a). Geller et al. (2017a) note that out of the seven RSS candidates they identify, four of them were found to be X-ray sources and three were found to be photometric or velocity variables. The three observations of each of these stars conducted to date, however, do not meet our velocity-variability threshold.

Geller et al. (2017b) suggest that SSGs and RSS may be linked through evolution; that is, SSGs may evolve into RSS. We might therefore expect these RSS candidates to be velocity variables, as are most SSGs, if the larger red stragglers can fit within the SSG orbits. We have obtained effective temperatures and luminosities of both WOCS 19016 and WOCS 22023 from *Gaia* DR2: WOCS 19016 has $T_{\text{eff}} = 4224\text{K}$ and $L = 73L_\odot$, while WOCS 22023 has $T_{\text{eff}} = 4531\text{K}$ and $L = 9.5L_\odot$. From these values we derive estimated stellar radii of 16 R_\odot and 5 R_\odot , respectively. Following the formalism of Paczyński (1971), we derive the minimum orbital periods of these two stars with the relation

$$\frac{R_{L1}}{a} = 0.38 + 0.2 \log_{10} \left(\frac{M_1}{M_2} \right), \quad (3)$$

where R_{L1} is the Roche lobe radius of the primary star. For each star we set R_{L1} equal to the derived radius of the star. Assuming each star is near the cluster turnoff with a mass of $\sim 1.8 M_{\odot}$ and each has a $1 M_{\odot}$ companion orbiting at the Roche radius, we find limiting orbital periods of ~ 17 d for WOCS 19016 and ~ 3 d for WOCS 22023. These periods are typical of SSGs (albeit perhaps not WOCS 20035 here), and so do not evidently explain the lack of velocity variability of these RSS candidates.

We also examine the respective critical separations for stability against tidal mergers, using the relation from [Rasio \(1995\)](#):

$$\frac{a_{\text{inst}}}{R_1} = \left[\frac{3(1+q)}{q} \right]^{1/2} k_1, \quad (4)$$

where q is defined to be M_2/M_1 , R_1 is the radius of the primary star, and k_1 is the dimensionless gyroradius of the primary star. If we assume $k_1^2 \sim 0.1$, as does [Webbink \(1976\)](#), the critical separation for each star corresponds to a period of ~ 120 d for WOCS 19016 and ~ 22 d for WOCS 22023, respectively, both substantially longer than the minimum periods at their Roche radii. We note that these results depend somewhat sensitively on the choice of k_1 . We also note that the relation of [Rasio \(1995\)](#) is a good approximation only for a mostly radiative main-sequence star. Stars with more substantial convective envelopes are more compressible than primarily radiative stars, which tends to shrink a_{inst} for a fixed primary radius. Presuming sub-subgiants and their descendants do have substantial convective envelopes, our derived a_{inst} could be too large by as much as $\sim 30\%$. It is therefore possible that these two stars are the result of merged sub-subgiants in close binaries, once the primary star began evolving along its RGB. Neither of these two stars, however, have been observed to be rapidly rotating, challenging the merger hypothesis. These two stars remain targets of ongoing study.

There are three other stars in the sub-subgiant and red straggler regions of the CMD: WOCS 24035, WOCS 29015, and WOCS 35029. All of these stars have high-noise astrometry, and as such we do not have reliable P_{μ} for them. These stars are placed on the CMD based solely on their P_{RV} , and none of them show velocity variability or unusually large radii. While these stars are also the subject of continued study, we do not label them as RSS or SSGs at this time because we cannot say with the same level of certainty that they are cluster members.

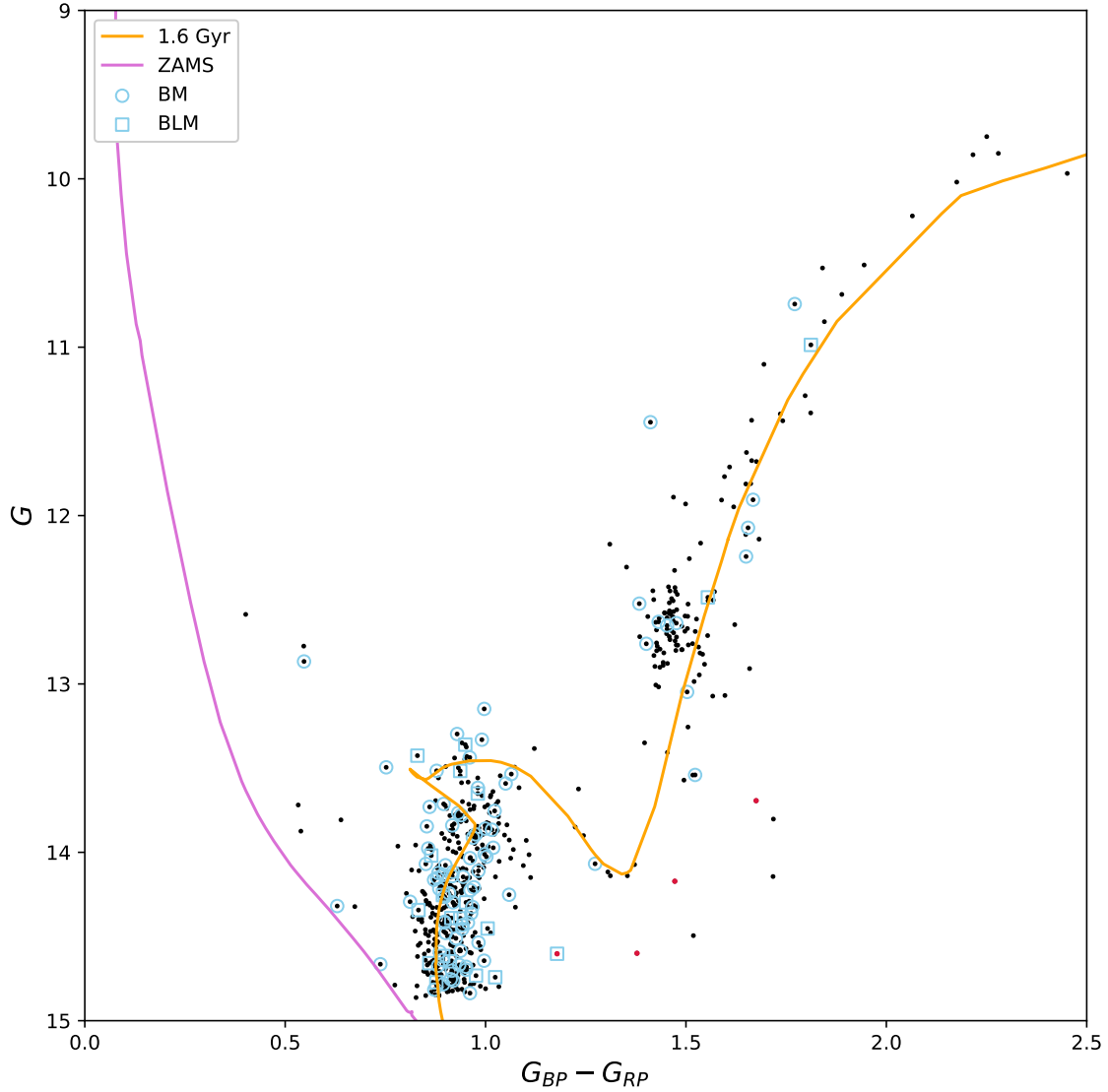


Figure 11. NGC 7789 CMD of all three-dimensional members (SM, BLM, and BM) and a few members determined only by RV (Section 6.4). Velocity-variable stars are indicated in blue, with circles for BMs with completed orbital solutions and squares for BLMs without completed orbital solutions. We overplot a 1.6 Gyr MIST (Dotter 2016) isochrone in orange with a distance of 1.8 kpc, $A_V = 0.85$, and $[\text{Fe}/\text{H}] = 0.023$, as well as a ZAMS in lavender with the same parameters. The SSGs and RSS discussed in Section 6.6 are marked with red points.

7. SPECTROSCOPIC BINARY ORBITS

7.1. *Single-Lined Orbital Solutions*

Using the data given in Table 1 we determine orbital solutions for 62 single-lined spectroscopic binaries (SB1). We show these orbit solutions in Figure 12. For each, the orbit solution is plotted in the top panel and the observed-minus-computed-residuals (O–C) are plotted in the bottom panel. The orbital elements and the 1σ errors for each binary are listed in Table 6. The first row contains the binary ID, the orbital period (P), the number of orbital cycles observed, the center-of-mass RV (γ), the orbital amplitude (K), the eccentricity (e), the longitude of periastron (ω), a Julian Date of periastron passage (T_o), the projected semi-major axis ($a \sin i$), the mass function ($f(m)$), the rms residual velocity from the orbital solution (σ), and the number of RV measurements (N). The second row contains the respective errors.

Table 6. Orbital Parameters for NGC 7789 Single-Lined Binaries

ID	P (days)	Orbital Cycles	γ (km s ⁻¹)	K (km s ⁻¹)	e	ω (deg)	T _o (HJD-2400000 d)	asin i (10 ⁶ km)	f(m) (M _⊙)	σ (km s ⁻¹)	N
1006	783.9 ± 2.3	2.3	-54.96 ± 0.18	14.3 ± 0.3	0.413 ± 0.014	54 ± 3	55421 ± 4	141 ± 3	1.81e-1 ± 1.2e-2	0.63	16
2001	58.581 ± 0.017	55.7	-52.5 ± 0.4	26.5 ± 0.6	0.151 ± 0.022	72 ± 6	55049.4 ± 1.0	21.1 ± 0.4	1.10e-1 ± 0.7e-2	1.75	36
4004	1546 ± 3	1.3	-55.09 ± 0.19	20 ± 5	0.90 ± 0.05	286 ± 6	55144 ± 4	190 ± 60	1.2e-1 ± 1.0e-1	0.39	26
4035	155.79 ± 0.04	13.4	-55.02 ± 0.10	26.77 ± 0.15	0.442 ± 0.004	50.8 ± 0.8	54693.2 ± 0.3	51.4 ± 0.3	2.23e-1 ± 0.4e-2	0.35	17
5008	217.3 ± 0.5	9.4	-54.77 ± 0.14	4.97 ± 0.20	0.06 ± 0.05	330 ± 40	55042 ± 22	14.8 ± 0.6	2.8e-3 ± 0.3e-3	0.51	15
5009	202.20 ± 0.03	24.9	-54.50 ± 0.09	21.48 ± 0.14	0.011 ± 0.006	140 ± 40	54500 ± 21	59.7 ± 0.4	2.07e-1 ± 0.4e-2	0.39	21
5010	451.0 ± 0.4	4.9	-54.51 ± 0.07	17.03 ± 0.10	0.262 ± 0.005	71.8 ± 1.4	55146.4 ± 1.6	101.9 ± 0.6	2.07e-1 ± 0.4e-2	0.20	13
5011	2710 ± 60	1.4	-53.78 ± 0.13	4.15 ± 0.20	0.32 ± 0.04	6 ± 9	55980 ± 60	147 ± 7	1.71e-2 ± 2.5e-3	0.67	34
7014	359.16 ± 0.23	14.0	-55.15 ± 0.14	12.30 ± 0.19	0.484 ± 0.011	262 ± 3	55093.9 ± 1.9	53.1 ± 0.9	4.64e-2 ± 2.2e-3	0.54	22
8007	55.563 ± 0.018	37.7	-54.28 ± 0.23	22.12 ± 0.20	0.168 ± 0.011	33 ± 4	55027.5 ± 0.6	16.66 ± 0.15	5.97e-2 ± 1.6e-3	0.56	15
8029	267.72 ± 0.22	3.3	-56.17 ± 0.05	14.07 ± 0.08	0.269 ± 0.005	289.4 ± 1.3	56962.3 ± 0.9	49.9 ± 0.3	6.90e-2 ± 1.2e-3	0.17	13
9011	680 ± 4	3.5	-54.4 ± 0.3	6.9 ± 0.4	0.05 ± 0.05	240 ± 60	54950 ± 120	64 ± 4	2.3e-2 ± 0.4e-2	0.76	19
10011	517 ± 6	5.5	-53.7 ± 0.3	6.5 ± 0.4	0.37 ± 0.07	79 ± 10	56773 ± 11	43 ± 3	1.19e-2 ± 2.3e-3	1.14	22
11017	13.7827 ± 0.0009	160.5	-53.21 ± 0.13	9.50 ± 0.15	0.053 ± 0.024	102 ± 19	55167.6 ± 0.8	1.80 ± 0.03	1.22e-3 ± 0.6e-4	0.46	17
12002	13.1721 ± 0.0008	217.2	-54.1 ± 0.5	46.7 ± 0.6	0.015 ± 0.018	130 ± 60	56546.5 ± 2.0	8.46 ± 0.12	1.39e-1 ± 0.6e-2	1.55	15
12004	9.4119 ± 0.0005	192.7	-54.5 ± 0.3	27.2 ± 0.4	0.044 ± 0.015	175 ± 18	54234.7 ± 0.5	3.52 ± 0.05	1.96e-2 ± 0.8e-3	1.06	17
12006	114.56 ± 0.03	18.2	-54.49 ± 0.16	18.34 ± 0.21	0.151 ± 0.013	73 ± 5	54636.8 ± 1.5	28.6 ± 0.3	7.08e-2 ± 2.4e-3	0.74	29
12007	85.509 ± 0.018	58.8	-54.8 ± 0.3	20.9 ± 0.4	0.064 ± 0.019	127 ± 18	54961 ± 4	24.6 ± 0.5	8.1e-2 ± 0.5e-2	1.34	27
13007	532.2 ± 1.4	9.4	-54.57 ± 0.16	8.2 ± 0.3	0.30 ± 0.03	68 ± 5	54913 ± 7	57.0 ± 1.9	2.6e-2 ± 0.3e-2	0.74	26

Table 6 continued on next page

Table 6 (*continued*)

ID	P	Orbital	γ	K	e	ω	T_o	asin i	f(m)	σ	N
	(days)	Cycles	(km s ⁻¹)	(km s ⁻¹)		(deg)	(HJD-2400000 d)	(10 ⁶ km)	(M _⊙)	(km s ⁻¹)	
13017	45.047	104.3	-53.42	11.3	0.20	340	55229.3	6.84	6.3e-3	0.77	15
	± 0.009		± 0.22	± 0.4	± 0.03	± 9	± 1.1	± 0.24	± 0.6e-3		
13021	205.8	17.8	-52.1	10.0	0.47	22	55522	25.1	1.5e-2	1.13	16
	± 0.3		± 0.3	± 0.6	± 0.04	± 11	± 7	± 1.7	± 0.3e-2		
14008	225.4	9.6	-55.28	7.79	0.02	310	54590	24.1	1.10e-2	0.68	17
	± 0.4		± 0.19	± 0.23	± 0.04	± 120	± 80	± 0.7	± 1.0e-3		
14011	1420	1.8	-52.08	6.1	0.73	143	55459	81	1.0e-2	0.80	18
	± 60		± 0.20	± 0.5	± 0.03	± 8	± 15	± 7	± 0.3e-2		
15012	56.360	83.3	-52.4	19.8	0.188	274	55761.2	15.1	4.30e-2	0.90	15
	± 0.014		± 0.3	± 0.3	± 0.020	± 6	± 0.9	± 0.3	± 2.3e-3		
15016	1840	1.4	-53.25	4.9	0.43	141	54180	111	1.6e-2	0.71	17
	± 60		± 0.23	± 0.5	± 0.07	± 8	± 70	± 11	± 0.5e-2		
16013	277.7	9.3	-54.11	4.8	0.33	54	56935	17.3	2.7e-3	0.47	14
	± 0.8		± 0.21	± 0.3	± 0.06	± 12	± 6	± 1.0	± 0.4e-3		
18003	3.09148	925.2	-54.66	27.6	0.148	299	56395.40	1.162	6.6e-3	0.74	15
	± 0.00005		± 0.25	± 0.5	± 0.012	± 5	± 0.04	± 0.020	± 0.3e-3		
18009	130.05	19.9	-54.8	13.3	0.27	313	56733.9	22.9	2.8e-2	0.91	14
	± 0.07		± 0.3	± 0.5	± 0.03	± 6	± 2.1	± 0.8	± 0.3e-2		
18015	57.105	45.4	-54.33	24.1	0.386	90.2	56778.1	17.48	6.5e-2	0.63	13
	± 0.017		± 0.18	± 0.3	± 0.011	± 2.3	± 0.3	± 0.24	± 0.3e-2		
18028	32.551	22.7	-51.81	21.07	0.289	234.8	56913.66	9.03	2.77e-2	0.14	14
	± 0.003		± 0.06	± 0.07	± 0.003	± 0.7	± 0.05	± 0.03	± 0.3e-3		
19008	2.62664	576.0	-53.8	30.6	0.006	270	54877.9	1.107	7.8e-3	1.30	22
	± 0.00003		± 0.3	± 0.4	± 0.016	± 110	± 0.8	± 0.016	± 0.3e-3		
19011	206.1	8.9	-55.31	3.0	0.44	72	56277	7.6	4.1e-4	0.95	17
	± 1.6		± 0.24	± 0.4	± 0.10	± 20	± 8	± 1.1	± 1.7e-4		
19019	7.1108	159.9	-53.50	10.85	0.148	160	56087.61	1.049	9.1e-4	0.42	12
	± 0.0003		± 0.14	± 0.22	± 0.018	± 8	± 0.15	± 0.022	± 0.6e-4		
20006	360.5	5.5	-52.9	14.5	0.50	25	55066	62	7.3e-2	1.83	16
	± 1.4		± 0.5	± 0.9	± 0.04	± 7	± 4	± 4	± 1.4e-2		
20009	4190	0.9	-56.21	4.5	0.27	11	58390	253	3.6e-2	1.19	44
	± 230		± 0.21	± 0.4	± 0.09	± 17	± 160	± 23	± 1.0e-2		
20014	16.5000	304.8	-54.5	10.4	0.05	20	55194.7	2.36	1.92e-3	0.98	19
	± 0.0015		± 0.3	± 0.3	± 0.03	± 50	± 2.3	± 0.07	± 1.7e-4		
21006	549.1	4.6	-56.8	21.1	0.657	38	54898	120	2.3e-1	1.20	17
	± 1.8		± 0.3	± 0.9	± 0.019	± 3	± 3	± 6	± 0.3e-1		
21010	24.1219	208.5	-54.04	21.46	0.017	80	55326	7.12	2.47e-2	0.78	21
	± 0.0015		± 0.19	± 0.25	± 0.013	± 40	± 3	± 0.08	± 0.9e-3		
22008	413.7	9.4	-52.2	7	0.79	231	55598	25	4.0e-3	1.19	24
	± 0.6		± 0.4	± 4	± 0.16	± 17	± 3	± 17	± 0.7e-2		
22010	9.05801	315.9	-54.58	20.33	0.019	72	56572.3	2.532	7.88e-3	0.39	14

Table 6 *continued on next page*

Table 6 (*continued*)

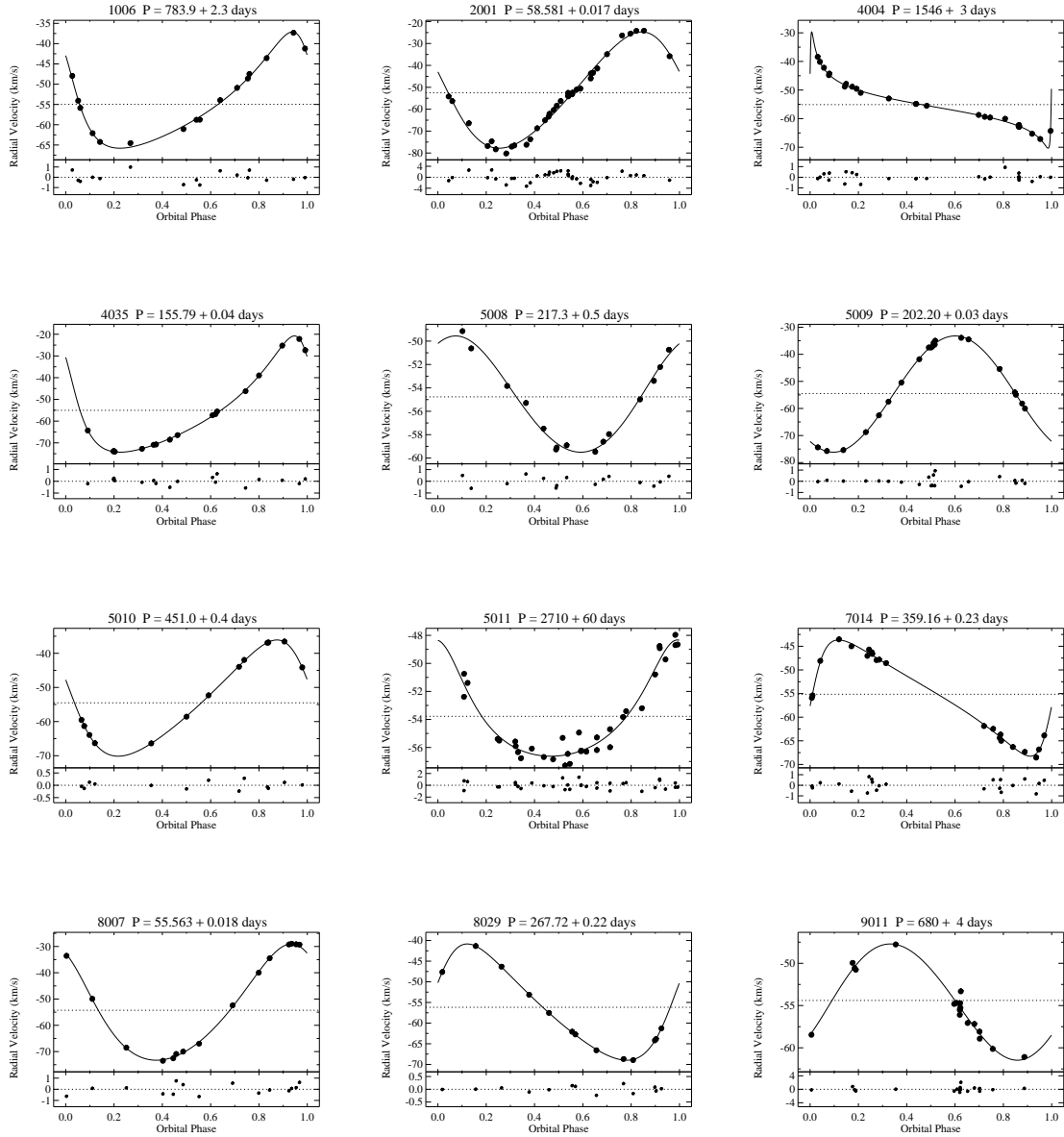
ID	P	Orbital	γ	K	e	ω	T_{\odot}	asin i	f(m)	σ	N
	(days)	Cycles	(km s ⁻¹)	(km s ⁻¹)		(deg)	(HJD-2400000 d)	(10 ⁶ km)	(M _⊙)	(km s ⁻¹)	
	± 0.00022		± 0.13	± 0.19	± 0.010	± 22	± 0.5	± 0.024	± 2.2e-4		
22018	1.883543	691.1	-51.4	34.8	0.038	6	56442.86	0.900	8.2e-3	0.97	12
	± 0.000019		± 0.3	± 0.5	± 0.019	± 17	± 0.09	± 0.013	± 0.3e-3		
24005	1054	4.8	-53.09	4.3	0.32	78	54920	59	7.2e-3	0.72	19
	± 15		± 0.18	± 0.3	± 0.06	± 13	± 40	± 4	± 1.4e-3		
24025	208.7	10.6	-54.2	10.4	0.27	307	55136	28.7	2.2e-2	0.98	17
	± 0.3		± 0.3	± 0.4	± 0.04	± 8	± 4	± 1.3	± 0.3e-2		
25015	50.58	25.5	-54.1	21.9	0.10	179	56335	15.1	5.4e-2	1.22	12
	± 0.03		± 0.5	± 0.6	± 0.03	± 20	± 3	± 0.4	± 0.5e-2		
26019	885	3.8	-53.71	5.9	0.34	339	57460	67	1.5e-2	1.08	31
	± 7		± 0.23	± 0.6	± 0.09	± 9	± 19	± 7	± 0.5e-2		
27008	735	2.3	-54.18	10.1	0.37	186	55893	95	6.2e-2	0.47	12
	± 3		± 0.16	± 0.5	± 0.04	± 5	± 8	± 5	± 0.9e-2		
27012	143.55	25.6	-53.3	13.9	0.31	53	55905.7	26.2	3.5e-2	0.91	14
	± 0.13		± 0.3	± 0.4	± 0.03	± 6	± 2.2	± 0.8	± 0.3e-2		
28010	277.1	14.9	-55.4	7.9	0.51	14	55402	26.0	9.1e-3	1.01	16
	± 0.4		± 0.3	± 0.5	± 0.04	± 7	± 3	± 1.7	± 1.7e-3		
28032	9.2830	113.5	-54.5	9.1	0.18	348	56465.5	1.14	6.9e-4	0.82	12
	± 0.0022		± 0.3	± 0.8	± 0.06	± 18	± 0.5	± 0.10	± 1.9e-4		
28035	3.825608	543.0	-55.2	58.4	0.006	190	54712.0	3.073	7.90e-2	1.54	29
	± 0.000025		± 0.3	± 0.4	± 0.007	± 80	± 0.9	± 0.021	± 1.6e-3		
29011	80.35	62.5	-53.93	10.1	0.19	42	55087.6	11.0	8.1e-3	0.67	16
	± 0.04		± 0.17	± 0.3	± 0.03	± 8	± 1.6	± 0.3	± 0.6e-3		
29022	13.8619	362.7	-54.5	33.3	0.007	210	54936	6.34	5.3e-2	1.72	31
	± 0.0003		± 0.4	± 0.7	± 0.017	± 110	± 4	± 0.13	± 0.3e-2		
31008	26.6262	82.7	-54.56	16.2	0.103	343	56334.2	5.90	1.15e-2	0.36	16
	± 0.0019		± 0.12	± 0.3	± 0.018	± 6	± 0.4	± 0.13	± 0.7e-3		
31025	2.57599	1823.0	-53.59	10.28	0.05	10	55158.94	0.364	2.89e-4	0.75	17
	± 0.00003		± 0.21	± 0.23	± 0.03	± 30	± 0.21	± 0.008	± 2.0e-5		
32009	46.76	88.5	-54.09	13.5	0.196	154	55585.5	8.49	1.11e-2	0.66	16
	± 0.03		± 0.21	± 0.3	± 0.023	± 8	± 1.2	± 0.21	± 0.8e-3		
33021	250.1	7.3	-54.02	7.3	0.46	6	55875	22.3	7.0e-3	0.66	15
	± 0.9		± 0.20	± 0.5	± 0.03	± 9	± 7	± 1.4	± 1.3e-3		
34028	48.414	97.0	-55.2	33.3	0.393	52	55374.1	20.4	1.44e-1	1.99	38
	± 0.006		± 0.4	± 0.8	± 0.018	± 3	± 0.3	± 0.5	± 1.1e-2		
35011	3.194552	1574.6	-52.2	37.5	0.058	13	55348.59	1.643	1.73e-2	1.12	25
	± 0.000010		± 0.3	± 0.4	± 0.008	± 11	± 0.10	± 0.017	± 0.5e-3		
35028	11.3078	415.2	-53.66	8.3	0.08	69	55289.3	1.29	6.7e-4	0.73	20
	± 0.0006		± 0.19	± 0.3	± 0.04	± 22	± 0.7	± 0.04	± 0.6e-4		
36011	217.6	17.9	-52.49	2.5	0.74	186	56029	5.0	1.1e-4	0.54	13
	± 0.4		± 0.17	± 0.3	± 0.09	± 14	± 6	± 1.0	± 0.5e-4		

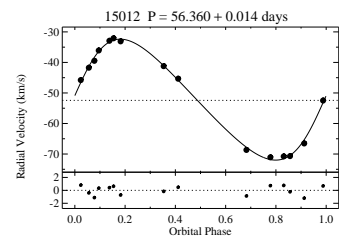
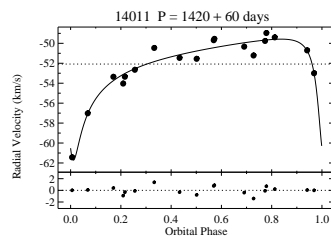
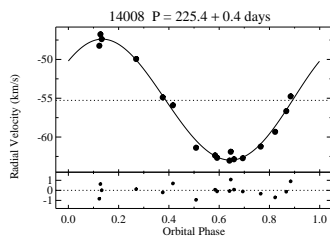
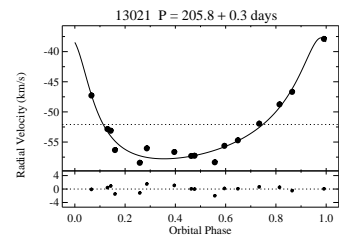
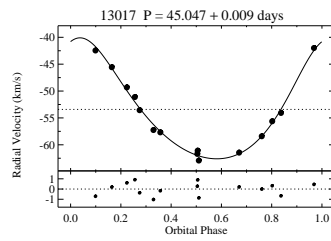
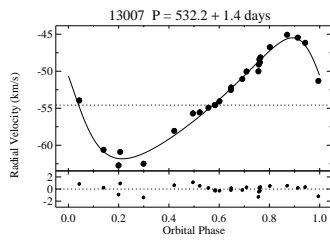
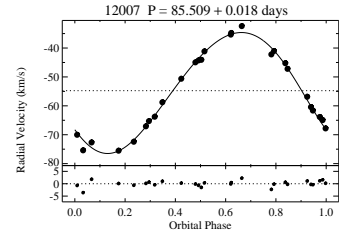
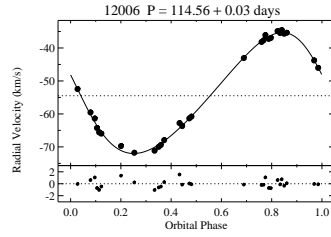
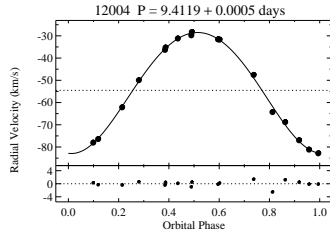
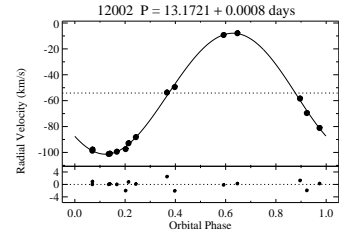
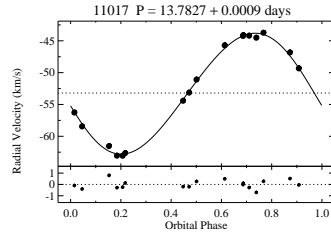
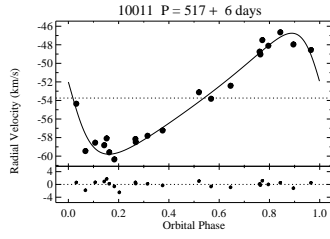
Table 6 continued on next page

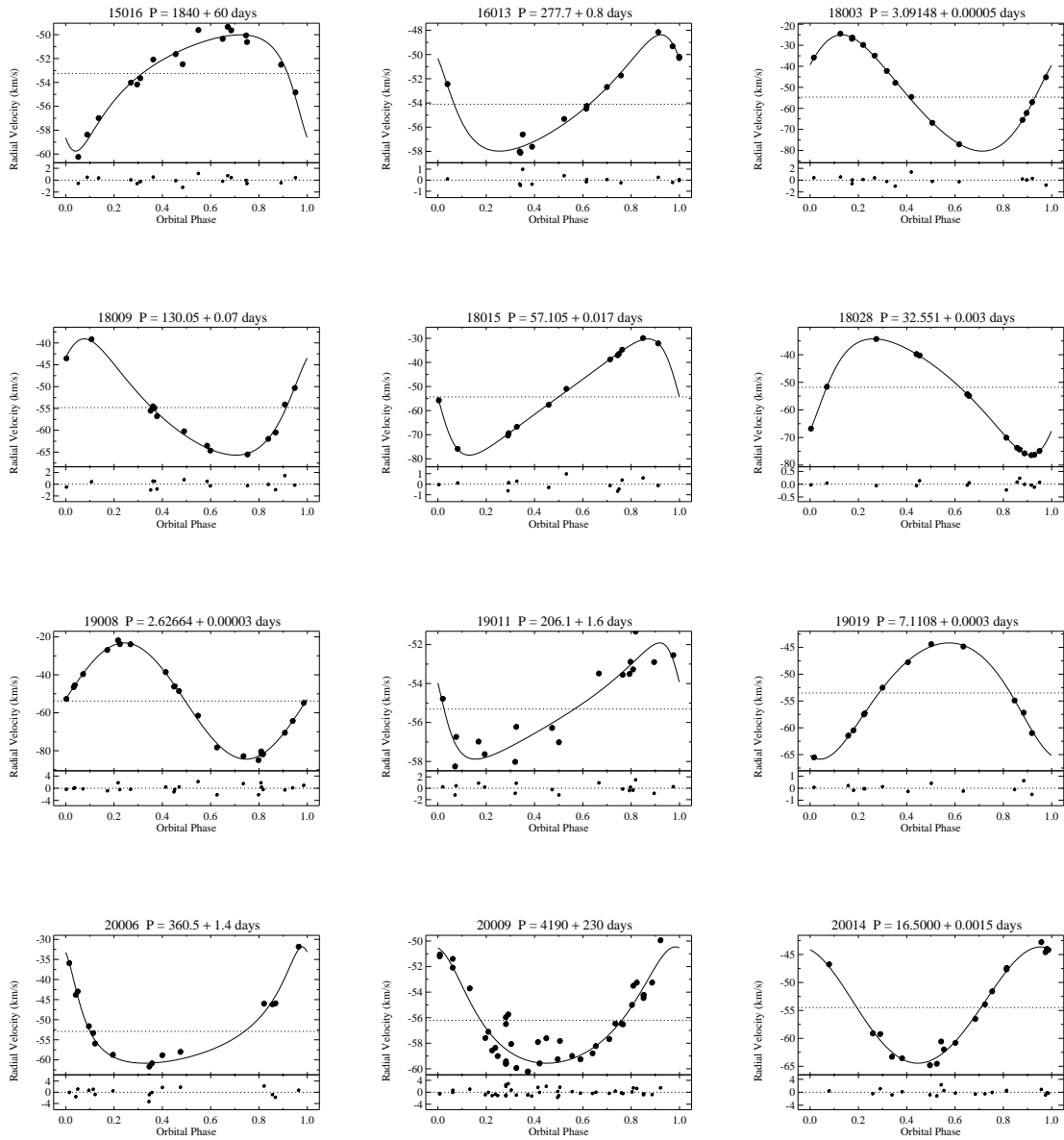
Table 6 (*continued*)

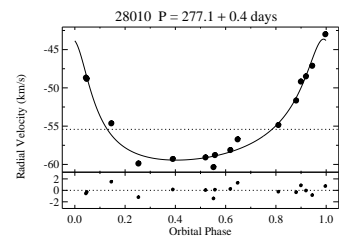
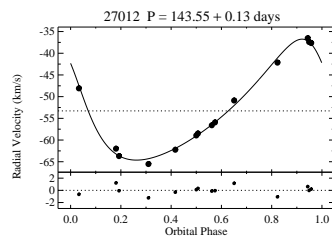
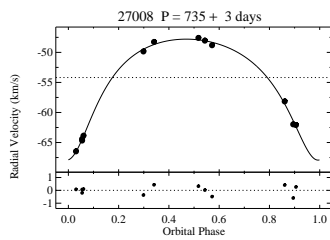
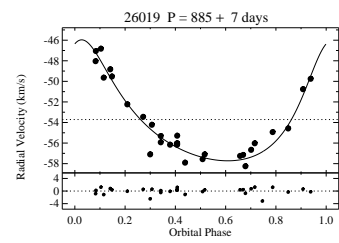
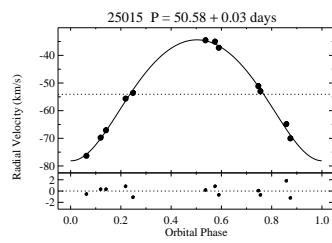
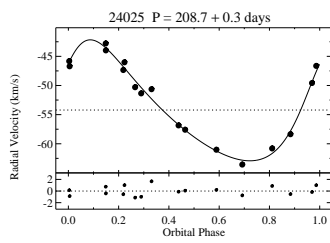
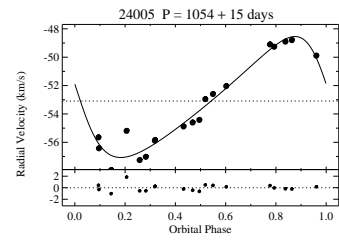
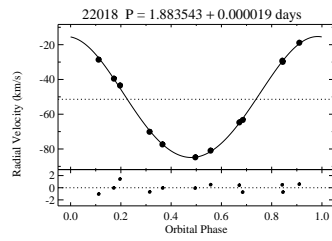
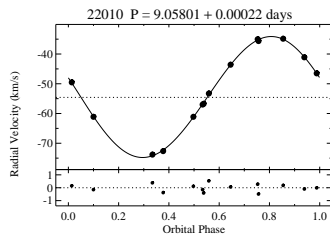
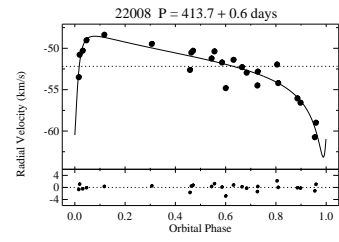
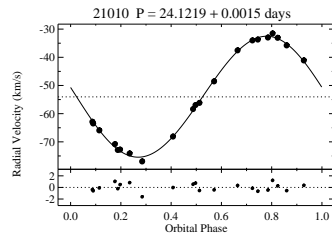
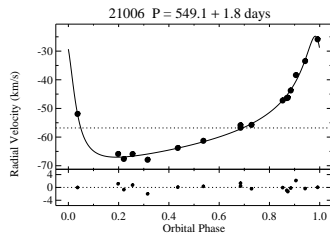
ID	P	Orbital	γ	K	e	ω	T_o	asin i	f(m)	σ	N
	(days)	Cycles	(km s ⁻¹)	(km s ⁻¹)		(deg)	(HJD-2400000 d)	(10 ⁶ km)	(M _⊙)	(km s ⁻¹)	
36016	444.9	7.5	-53.7	11.5	0.64	142	55864	54	3.1e-2	1.39	17
	± 1.5		± 0.4	± 0.7	± 0.03	± 5	± 3	± 4	± 0.6e-2		
47010	46.706	103.6	-54.3	22.5	0.68	237	55374.74	10.6	2.2e-2	1.58	21
	± 0.019		± 0.4	± 1.1	± 0.03	± 3	± 0.21	± 0.6	± 0.4e-2		

NOTE—Table 6 is also published in machine-readable format.









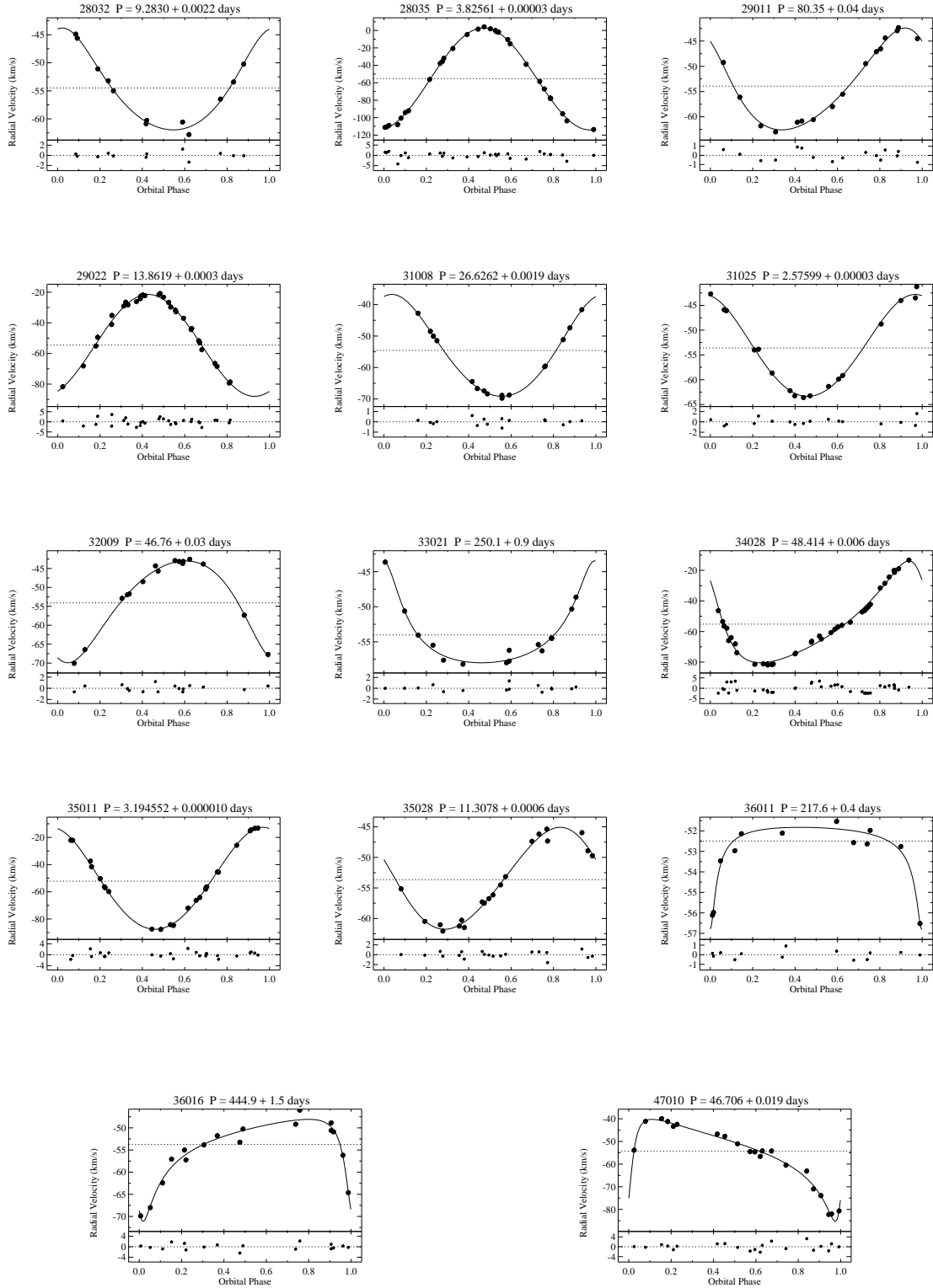


Figure 12. NGC 7789 SB1 orbit plots. We plot RV against orbital phase for each binary with the WOCS ID and orbital period above each plot. Filled circles indicate the data points, the solid line is the orbital fit to the data, and the dotted line marks the γ -velocity. We show the residuals from the fit below each binary plot.

7.2. *Double-Lined Orbital Solutions*

For double-lined spectroscopic binaries (SB2) we use TODCOR (Zucker & Mazeh 1994) which utilizes two template spectra to simultaneously derive RVs for the primary and secondary stars. For these binaries we used an observed solar spectrum for both templates.

We plot the SB2 orbital solutions in Figure 13. The top panel shows the primary RVs (filled circles) and fitted solution (solid line), the secondary RVs (open circles) and fitted solution (dashed line), as well as the γ velocity (dotted line). Square symbols (\square) represent data where the difference in velocities were below our spectral resolution of 20 km s^{-1} , and were therefore not included in our orbital solutions. The bottom panel shows the O–C residuals for the primary (filled circles) and secondary (open circles). Table 7 lists the orbital elements and the 1σ errors for each SB2. In the first row is the binary ID, the orbital period (P), the number of orbital cycles observed, the center-of-mass RV (γ), the orbital amplitude of the primary (K), the eccentricity (e), the longitude of periastron (ω), a Julian Date of periastron passage (T_o), the projected primary semi-major axis ($a \sin i$), $m \sin^3 i$, the mass ratio (q), the rms residual velocity for the primary from the orbital solution (σ), and the number of RV measurements used in the orbital solutions after excluding measurements where the two velocities could not be resolved (N). The second row contains the respective errors on each of these values. The third and fourth rows are the amplitude (K), projected semi-major axis ($a \sin i$), $m \sin^3 i$, the rms residual velocity from the orbital solution (σ), and the number of resolved RV measurements (N) for the secondary star and the respective errors.

Table 7. Orbital Parameters For NGC 7789 Double-Lined Binaries

ID	P (days)	Orbital Cycles	γ (km s ⁻¹)	K (km s ⁻¹)	e	ω (deg)	T_0 (HJD-2400000 d)	$a \sin i$ (10 ⁶ km)	$m \sin^3 i$ (M _⊙)	q	σ (km s ⁻¹)	N
7003	30.627 ±0.005	66.5 ...	-53.8 ±0.3	38.1 ±0.6	0.415 ±0.012	108 ±2	55064.24 ±0.14	14.59 ±0.24	0.626 ±0.025	0.919 ±0.020	1.68 ...	21 ...
	41.4 ±0.7	15.9 ±0.3	0.575 ±0.022	...	1.91 ...	21 ...
8003	11.7576 ±0.0003	399.2 ...	-54.78 ±0.24	51.1 ±0.4	0.011 ±0.006	80 ±40	55045 ±1	8.26 ±0.07	0.677 ±0.016	0.981 ±0.013	1.43 ...	26 ...
	52.1 ±0.5	8.43 ±0.09	0.663 ±0.013	...	1.99 ...	26 ...
8016	30.9783 ±0.0005	151.6 ...	-52.4 ±0.1	52.3 ±0.1	0.393 ±0.002	308.7 ±0.5	55313.130 ±0.025	20.52 ±0.07	1.73 ±0.06	0.913 ±0.015	0.34 ...	15 ...
	57.4 ±0.8	22.5 ±0.4	1.58 ±0.03	...	2.55 ...	15 ...
9020	5.50869 ±0.00005	852.8 ...	-54.59 ±0.24	79.1 ±0.4	0.137 ±0.004	213 ±2	54878.02 ±0.03	5.94 ±0.03	1.26 ±0.04	0.936 ±0.014	1.23 ...	29 ...
	84 ±1	6.34 ±0.09	1.175 ±0.022	...	3.96 ...	29 ...
14007	23.167 ±0.001	217.2 ...	-53.0 ±0.3	38 ±1	0.219 ±0.022	227 ±4	54571.61 ±0.23	11.9 ±0.3	0.61 ±0.05	0.905 ±0.023	1.25 ...	17 ...
	42 ±1	13.1 ±0.4	0.55 ±0.04	...	2.33 ...	17 ...
14014	2.36601 ±0.00001	1748.0 ...	-51.6 ±0.7	107.5 ±0.9	0.020 ±0.009	94 ±26	55371.60 ±0.17	3.50 ±0.03	1.58 ±0.07	0.880 ±0.019	2.87 ...	19 ...

Table 7 continued on next page

Table 7 (continued)

ID	P (days)	Orbital Cycles	γ (km s ⁻¹)	K (km s ⁻¹)	e	ω (deg)	T_o (HJD-2400000 d)	$a \sin i$ (10 ⁶ km)	$m \sin^3 i$ (M _⊙)	q	σ (km s ⁻¹)	N
	122.2	3.97	1.39	...	7.68	19
	± 2.2	± 0.08	± 0.04
14022	11.5494	180.1	-53.5	33.9	0.015	40	54550	5.38	0.201	0.960	1.13	22
	±0.0003	...	± 0.2	±0.3	± 0.009	± 30	± 1	± 0.06	± 0.005	± 0.014
	35.2	5.60	0.193	...	1.23	22
	± 0.4	± 0.06	± 0.005
17008	2.76075	1701.8	-53.8	78.6	0.007	40	55011.4	2.984	1.070	0.730	1.85	23
	±0.00001	...	± 0.4	±0.5	± 0.006	± 50	± 0.4	± 0.021	± 0.021	± 0.008
	107.7	4.09	0.781	...	3.13	23
	± 0.8	± 0.04	± 0.013
17023	191.64	8.6	-52.6	27.1	0.401	176	57035	65.5	1.18	1.02	1.73	14
	±0.23	...	± 0.3	±0.5	± 0.012	± 6	± 2	± 1.7	± 0.06	± 0.03
	26.7	64.4	1.20	...	1.18	14
	± 0.4	± 1.2	± 0.07
17028	3.553964	1415.9	-56.5	86.9	0.119	166	54711.71	4.22	1.89	0.717	3.86	24
	±0.000014	...	± 0.6	±1.5	± 0.014	± 5	± 0.04	± 0.07	± 0.08	± 0.014
	121.2	5.88	1.39	...	5.28	24
	± 2.0	± 0.10	± 0.06
21025	3.555133	1227.0	-52.8	74.9	0.106	37	56430.56	3.64	0.880	0.84	2.53	35
	±0.000011	...	± 0.3	±0.6	± 0.006	± 3	± 0.03	± 0.03	± 0.017	± 0.01
	89.7	4.36	0.735	...	3.18	35
	± 0.7	± 0.04	± 0.013
23012	8.06720	354.4	-53.39	63.89	0.009	330	56378.9	7.09	1.367	0.803	1.50	12
	±0.00013	...	± 0.21	±0.52	± 0.004	± 20	± 0.4	± 0.07	± 0.016	± 0.008

Table 7 continued on next page

Table 7 (continued)

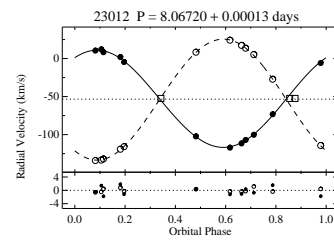
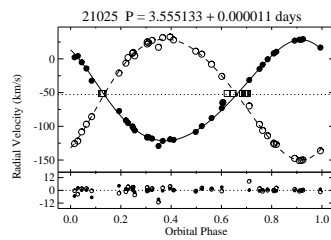
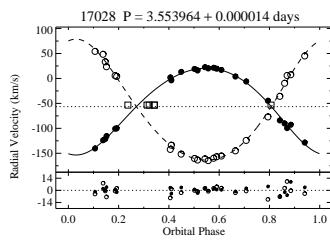
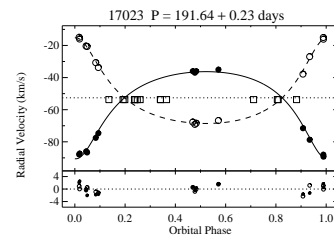
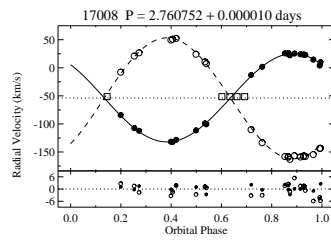
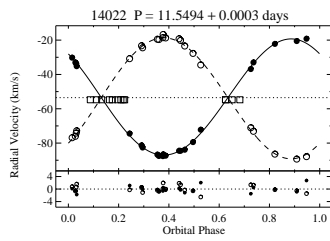
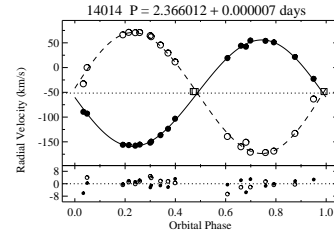
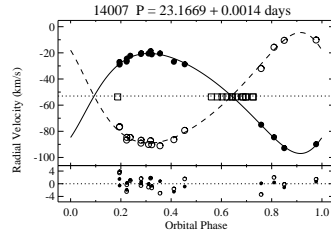
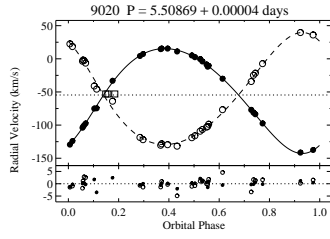
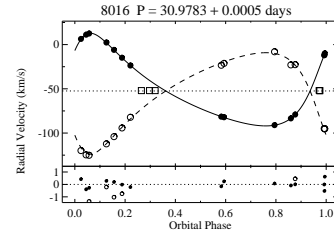
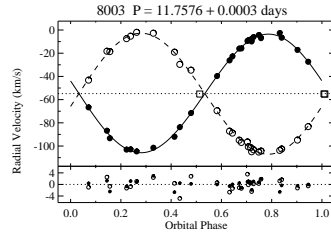
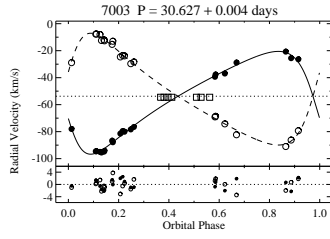
ID	P (days)	Orbital Cycles	γ (km s ⁻¹)	K (km s ⁻¹)	e	ω (deg)	T_o (HJD-2400000 d)	$a \sin i$ (10 ⁶ km)	$m \sin^3 i$ (M _⊙)	q	σ (km s ⁻¹)	N
	79.53	8.82	1.099	...	0.64	12
	± 0.24	± 0.03	± 0.021
29010	32.886	56.8	-51.9	37.6	0.522	91	56904.30	14.50	0.57	0.888	1.98	16
	±0.004	...	± 0.4	±0.9	± 0.012	± 2	± 0.14	± 0.34	± 0.03	± 0.025
	42.34	16.3	0.51	...	2.04	16
	± 0.98	± 0.4	± 0.03
30007	48.98	53.6	-51.2	33.6	0.23	173	57123	22.0	0.952	0.87	4.91	29
	±0.05	...	± 0.7	±1.6	± 0.04	± 9	± 1	± 1.0	± 0.114	± 0.05
	38.8	25.4	0.83	...	6.07	29
	± 1.9	± 1.2	± 0.09
31015	34.4144	95.3	-53.16	44.0	0.364	60	55558.35	19.38	1.081	0.952	0.62	16
	±0.0008	...	± 0.16	±0.4	± 0.009	± 1	± 0.07	± 0.13	± 0.023	± 0.011
	46.2	20.36	1.029	...	1.09	16
	± 0.5	± 0.20	± 0.018
32012	89.49	30.3	-55.3	36.4	0.573	99	57120.5	36.8	1.16	0.92	1.46	19
	±0.01	...	± 0.3	±0.8	± 0.010	± 3	± 0.4	± 0.7	± 0.08	± 0.03
	39.4	39.8	1.07	...	2.66	19
	± 1.1	± 1.1	± 0.06
34016	18.17561	276.7	-54.92	50.77	0.351	205.8	55639.781	11.88	1.013	0.895	0.25	14
	±0.00007	...	± 0.08	±0.11	± 0.002	± 0.5	± 0.018	± 0.03	± 0.013	± 0.006
	56.72	13.27	0.907	...	0.84	14
	± 0.30	± 0.08	± 0.007
35019	18.6780	125.8	-52.6	48.6	0.200	52	56098.16	12.24	1.5	0.767	1.39	14
	±0.0019	...	± 0.4	±0.6	± 0.011	± 3	± 0.16	± 0.17	± 0.1	± 0.024

Table 7 continued on next page

Table 7 (continued)

ID	P (days)	Orbital Cycles	γ (km s ⁻¹)	K (km s ⁻¹)	e	ω (deg)	T_o (HJD-2400000 d)	$a \sin i$ (10 ⁶ km)	$m \sin^3 i$ (M _⊙)	q	σ (km s ⁻¹)	N
	63.5	16.0	1.11	...	4.12	14
	± 1.6	± 0.5	± 0.05
35021	22.03877	96.5	-54.4	47.90	0.257	44	56601.18	14.03	1.33	0.828	0.52	12
	±0.00007	...	± 0.2	±0.21	± 0.005	± 1	± 0.08	± 0.07	± 0.03	± 0.009
	57.8	16.94	1.104	...	1.41	12
	± 0.5	± 0.18	± 0.018
37008	2.498732	1751.3	-53.64	64.00	0.021	24	54975.3	2.199	0.599	0.685	1.30	22
	±0.000006	...	± 0.32	±0.36	± 0.008	± 15	± 0.1	± 0.014	± 0.015	± 0.009
	93.43	3.21	0.410	...	3.53	22
	± 0.95	± 0.04	± 0.007
40008	27.9376	179.9	-53.2	46.8	0.290	128	55230.117	17.22	1.364	0.876	2.08	33
	±0.0012	...	± 0.2	±0.5	± 0.006	± 2	± 0.112	± 0.18	± 0.025	± 0.011
	53.4	19.65	1.20	...	1.65	33
	± 0.4	± 0.15	± 0.03

NOTE—Table 7 is also published in machine-readable format.



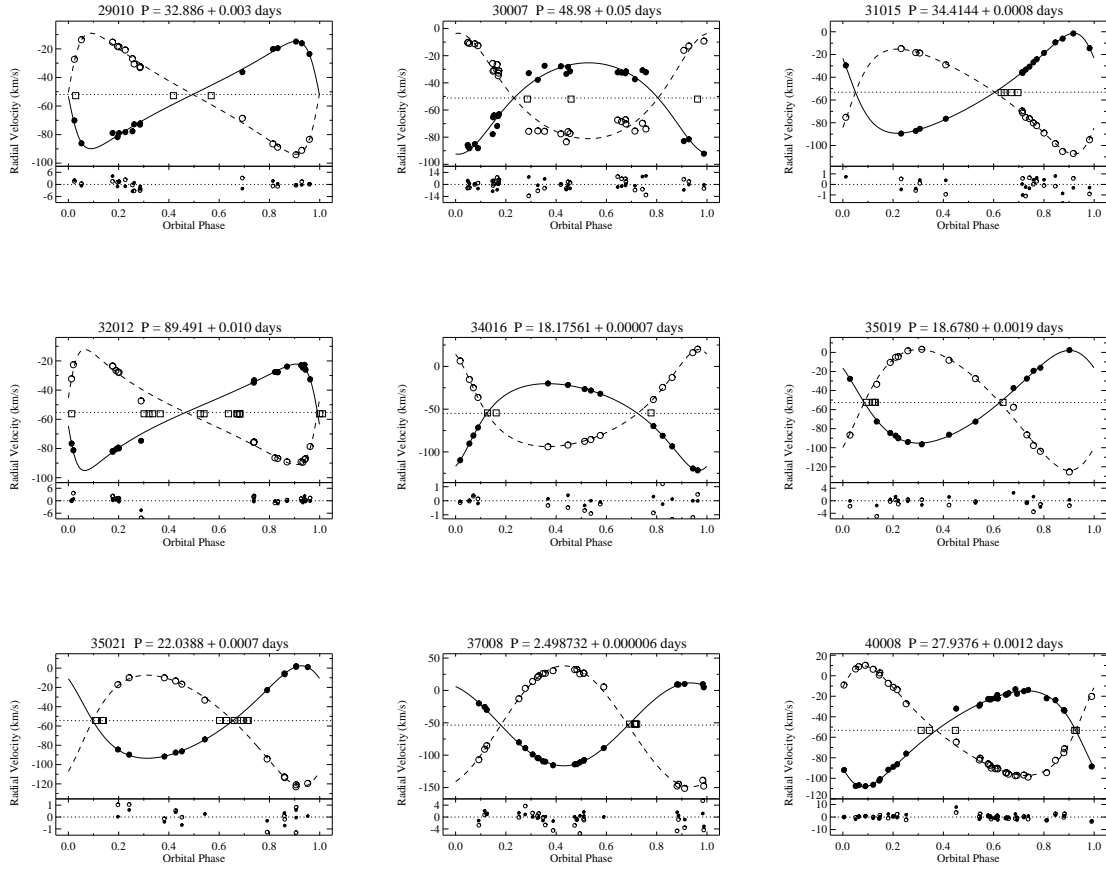


Figure 13. NGC 7789 SB2 orbit plots. We plot RV against orbital phase for each binary with the WOCS ID and orbital period above each plot. The data points and orbital fits for the primary star are represented by filled circles and a solid line. For the secondary star open circles and a dashed line represent the data points and the orbital fit, respectively. We mark the γ -velocity with a dotted line. We show the residuals from the fit below each binary plot, using the same symbols.

8. BINARY FREQUENCY

8.1. *Completeness in Binary Detection*

We follow the Monte Carlo approach to our binary detection completeness described in Geller & Mathieu (2012). In brief, we generate observations of artificial binaries based on the Galactic field binary period and eccentricity distributions of Raghavan et al. (2010) and a random selection of mass ratio, orbital inclination, ω , and phase. We incorporate the measured tidal circularization period of NGC 7789 determined in Section 10. For each star we use the actual observation dates and precision value based on its $v \sin i$. From the detectability of these synthetic binaries we calculated a detection percentage of 84% for binaries with periods under 1,000 days, 75% for periods under 3,000 days, and 60% for periods under 10,000 days. These numbers are slightly less than the completeness percentages for NGC 188 (Geller & Mathieu 2012) and NGC 6819 (Milliman et al. 2014). This is due to the poorer precision associated with the rapidly rotating stars, which makes it more difficult to identify long-period, low-amplitude binary stars.

8.2. *Main-Sequence Binary Frequency*

We find 226 single and 54 binary member and likely member stars on the main sequence of NGC 7789, restricting our analysis to $G \geq 14.0$ and $0.8 \leq G_{BP} - G_{RP} \leq 1.0$. We incorporate the 60% detection percentage to find a MS binary frequency of $31\% \pm 3\%$ for binaries with periods less than 10^4 days. This is consistent with the binary frequency of 32% found by Gim et al. (1998b) in their RV study of giant stars in NGC 7789.

The $P < 10^4$ d binary frequency found for other WOCS clusters include: $24\% \pm 3\%$ in M35 (150 Myr; Leiner et al. 2015), $22\% \pm 3\%$ in NGC 6819 (2.5 Gyr; Milliman et al. 2014), $34\% \pm 3\%$ in M67 (4 Gyr; Geller et al. 2020, in prep.), and $29\% \pm 3\%$ in NGC 188 (7 Gyr; Geller & Mathieu 2012). NGC 7789's value is consistent with these clusters.

9. PHOTOMETRIC VARIABLES

We have cross-referenced our primary sample to the photometric variables found by Jahn et al. (1995), Mochejska & Kaluzny (1999), and Zhang et al. (2003), and list the results in Table 8. Along with the photometric types and periods determined by these sources, we also list the orbital period for spectroscopic binaries, the P_{RV} , P_{μ} , and any additional comments we have for the star.

Table 8. NGC 7789 Photometric Variables

WOCs	Orbital	Jahn et al. (1995)	Mochejska & Kaluzny (1999)	Zhang et al. (2003)	P_μ	Comments			
ID	Period (d)	ID	Type	Period (d)	ID	Type	Period (d)	(%)	
7029	v12	EW	0.3917	0	VRR
11016	2.27414*	2.1077	0	BNM, SB1, RR, BSS Cand.
13004	...	V1	EW	1.1614	V1	100	BU, RR
14014	2.36601	1.2007	V10	96	BM, SB2
17028	3.553964	v30	EA	...	100	BM, SB2
20007	...	V13	98	BU
25008	...	V10	δ Scu	0.0868	81	SM, RR, BSS Cand.
33005	...	V2	EW	0.7165	VRR
33010	...	V6	EW	0.884	0	SNM

NOTE—EA: β Persei type (semi-detached), EB: β Lyrae type (detached), EW: W Ursae Majoris type (contact)

*While this binary is considered a field star, we have a complete orbital solution for it and provide its parameters as follows: $P = 2.27414 \pm 0.00003$ d, $\gamma = -56.5 \pm 0.4$ km s $^{-1}$, $K = 17.5 \pm 0.5$ km s $^{-1}$, $e = 0.07 \pm 0.03$, $\omega = 90 \pm 30$ deg, $T_0 = 55596.82 \pm 0.16$, $a \sin i = (0.547 \pm 0.015) \times 10^6$ km, $f(m) = 1.26e-3 \pm 0.11e-3$ M $_{\odot}$, $\sigma = 1.598$ km s $^{-1}$, $N = 23$.

Of the nine photometric variables that overlap with our primary NGC 7789 sample, we find three to be PM and RV members or likely members. WOCS 14014 and WOCS 17028, noted as eclipsing binaries by Mochejska & Kaluzny (1999) and Zhang et al. (2003), respectively, are SB2's with orbital solutions. The orbital period we find for WOCS 17028 is almost twice the eclipse period found by Mochejska & Kaluzny (1999). Zhang et al. (2003) do not fit a period to WOCS 14014 because of their short observing window and incomplete phase coverage. Another eclipsing binary, WOCS 11016, is an SB1 BSS candidate that has $P_\mu = 0\%$ and we consider it a field star. WOCS 13004 and WOCS 33005 are noted as W UMa's. WOCS 13004 has a very high proper-motion membership probability, and we also classify it as a BU RR with $v \sin i = 110 \text{ km s}^{-1}$. WOCS 33005 is a VRR with high-noise proper motion membership information. WOCS 20007 is detected by Jahn et al. (1995), but they did not have the time baseline to determine specifics about this system. We find it to be a binary which we classify as a BU. The one pulsating variable in this sample is a δ Scuti, WOCS 25008, which we find to be a single member of NGC 7789.

10. TIDAL CIRCULARIZATION

We update the standard WOCS method to measure the tidal circularization period (CP) for NGC 7789. Like Meibom & Mathieu (2005), we fit the piecewise function

$$e(P) = \begin{cases} 0.0 & \text{if } P \leq P', \\ \alpha (1 - e^{\beta(P'-P)})^\Gamma & \text{if } P > P' \end{cases} \quad (5)$$

to the period-eccentricity distribution of MS binaries from 1 mag below the cluster turnoff to our magnitude limit of $G \sim 15$ (excluding proper-motion non-members), using the same cutoffs as in Section 8. Γ is set to 1.0, β is set to 0.14, and α is set to 0.35, the average eccentricity for binary orbits over 50 days in the Pleiades, M35, Hyades, M67, and NGC 188. We minimize the total absolute deviation between the observed eccentricity and the model to determine the circularization function and P' . Specifically, we follow Geller et al. (2020, in prep.) and use a bootstrap technique to determine the circularization period and its uncertainties. CP is the period at which the best-fit circularization function equals 0.01, or $e(\text{CP}) = 0.01$.

We find a CP of $8.22^{+3.51}_{-1.35}$ days, and plot the period-eccentricity distribution along with the best-fit circularization function in Figure 14.

Meibom & Mathieu (2005) studied eight main-sequence binary populations: the pre-main-sequence, Pleiades, M35, Hyades, M67, NGC 188, the field, and the halo to investigate tidal dissipation mechanisms. Since then the tidal circularization of NGC 6819 was measured by Milliman et al. (2014), Leiner et al. (2015) updated the value for M35, and Geller et al. (2020, in prep.) updated the value for M67. With this work we incorporate the results for NGC 7789 and plot all the data in Figure 15. (But note that only the NGC 7789 and M67 data are derived with the new bootstrap algorithm. This approach finds larger uncertainties than found by Meibom & Mathieu 2005).

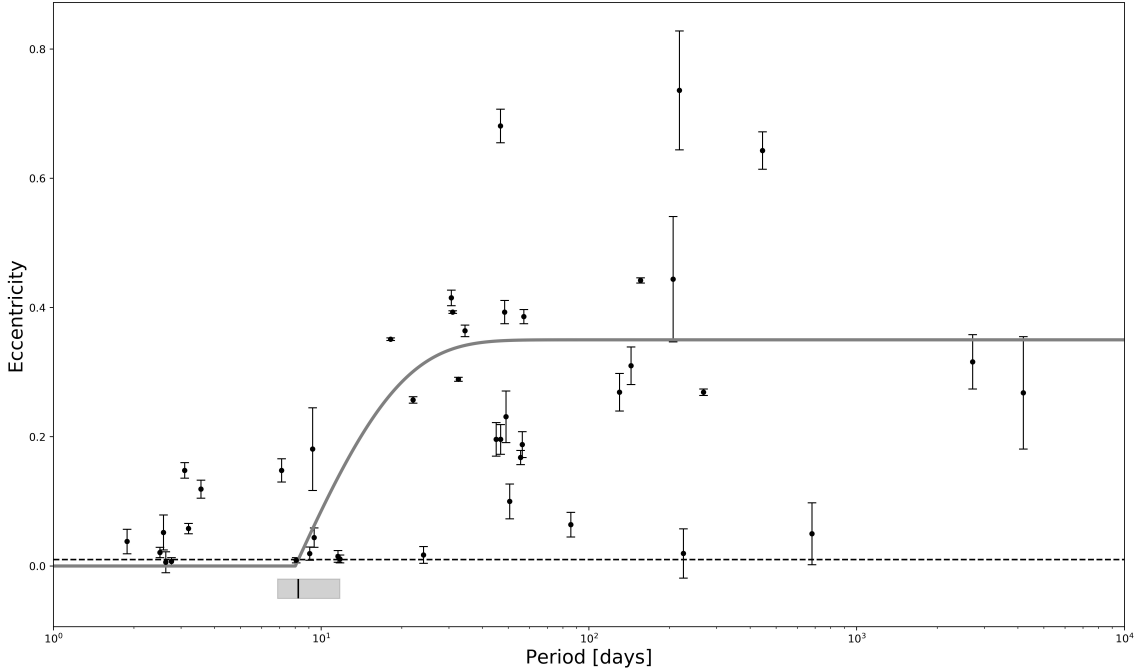


Figure 14. The orbital eccentricity versus the orbital period for the MS binaries in NGC 7789. The large eccentricities for long period systems transition to circular orbits for short period binaries. We determine the circularization period to be $8.22^{+3.51}_{-1.35}$ days indicated by a black dash near the bottom of the plot, with the uncertainty overplotted as a light grey bar. We also overplot the best-fit circularization function of Meibom & Mathieu (2005) in grey.

Our tidal circularization period for NGC 7789 is consistent with the trends of the prior clusters. It is worth reminding that the tidal circularization periods of both NGC 6819 and NGC 7789 are derived from main-sequence stars that have moved off of the cluster ZAMS, and are of slightly higher mass than the other clusters. Tidal circularization depends sensitively on stellar radius and convection zone structure. Future studies should re-determine the tidal circularization periods for these clusters with ZAMS stars.

We also include the theoretical predictions that tidal circularization is only significant during the pre-main-sequence (PMS) phase (Zahn & Bouchet 1989), the algorithm from the Binary-Star Evolution (BSE) code (Hurley et al. 2002) and an ad hoc rate from Geller et al. (2013) that combines the PMS circularization from Kroupa (1995) and the BSE from Hurley et al. 2002 with an artificially increased convective damping term tuned to match the distribution of tidal circularization period with cluster age. Still, no self-consistent theory is able to explain the relationship between cluster age and tidal circularization.

11. BLUE STRAGGLERS

We define BSS as being to the blue of the dashed line in Figure 16, which we place based on single-star and equal-mass binary isochrones. We list all the BSS in our pri-

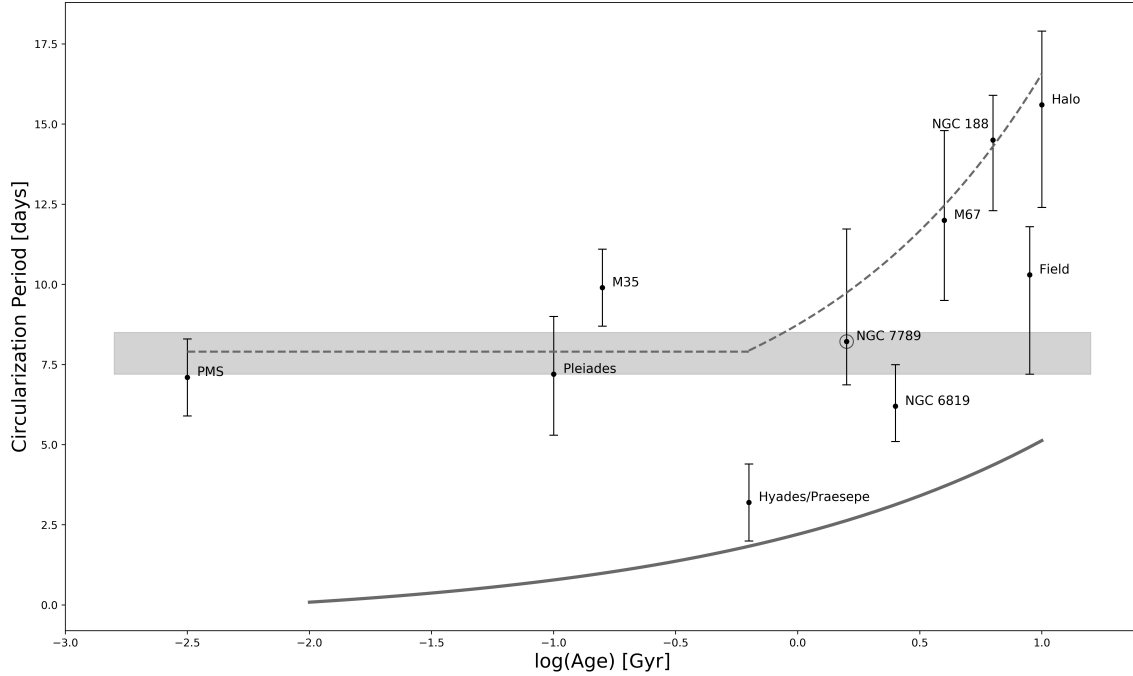


Figure 15. Tidal circularization period as a function of age for the eight clusters studied by Meibom & Mathieu (2005) including the update to M35 from Leiner et al. (2015), the addition of NGC 6819 from Milliman et al. (2014) and our result for NGC 7789. The Zahn & Bouchet (1989) prediction that tidal circularization is only significant during the PMS phase is plotted in the broad gray line. The theoretical model from the BSE algorithm from Hurley et al. (2002) and the ad hoc tidal energy dissipation rate from Geller et al. (2013) are also plotted as the solid gray curve and the dashed line, respectively.

mary NGC 7789 sample in Table 9 along with the number of WIYN observations that satisfy our quality thresholds, *Gaia* DR2 photometry, P_{RV} , P_{μ} , our RV membership classifications, as well as any additional comments.

Table 9. NGC 7789 Blue Straggler Candidates

WOCS ID	N	G	$G_{BP} - G_{RP}$	P_{RV}	P_{μ}	Class	Comment
<i>RV and PM members:</i>							
5004	14	12.78	0.55	95	99	SM	...
5011	34	12.87	0.55	95	99	BM	RR
9027	7	13.02	0.53	94	99	SM	RR
10010	9	13.72	0.53	95	96	SM	...
15015	9	13.87	0.54	95	99	SM	...
16020	18	13.81	0.64	95	99	SM	...
20009	42	14.32	0.63	62	99	BM	...
25008 [*]	13	13.96	0.78	94	81	SM	RR
25024 [*]	11	14.79	0.77	94	99	SM	RR

Table 9 continued on next page

Table 9 (*continued*)

WOCS ID	N	G	$G_{BP} - G_{RP}$	P_{RV}	P_{μ}	Class	Comment
27010	14	14.32	0.67	94	99	SM	...
36011	13	14.66	0.74	94	98	BM	...
<i>RV members with high-noise PM information:</i>							
4009 [*]	15	12.59	0.40	92	...	SM	...
10011 [*]	22	13.50	0.75	96	...	BM	...
<i>RV members and PM non-members:</i>							
8022	31	13.35	0.65	93	29	BNM	...
11015	13	13.35	0.53	70	0	SNM	Hot
11016	25	13.79	0.65	65	0	BNM	RR
13016	14	13.81	0.77	87	0	SNM	...
20012	12	14.37	0.69	95	0	SNM	...
24034	12	14.44	0.75	95	0	SNM	...
37005	12	14.89	0.79	86	17	BNM	...
<i>RV non-members and PM members:</i>							
1014	18	11.98	0.42	5	99	SNM	RR
3024	7	12.30	0.56	0	94	SNM	RR

^{*}These are the BSS marked as borderline as discussed in Section 11, whether by proximity to our cutoff or by astrometric noise.

Eleven BSS have $P_{RV} \geq 50\%$ and $P_{\mu} \geq 50\%$, and two more BSS have $P_{RV} \geq 50\%$ but high-noise PM information. We consider these 13 stars to be BSS cluster members. Seven other BSS with $P_{RV} \geq 50\%$ all have $P_{\mu} < 50\%$ and we treat them as field stars. For the member BSS, four have completed orbital solutions: WOCS 5011, WOCS 10011, WOCS 20009, and WOCS 36011. All of these stars are SB1s. WOCS 5011 and WOCS 20009 are both long-period SB1s with periods of 2710 d and 4190 d, respectively. Such periods are consistent with mass transfer from asymptotic branch giants (e.g., Geller & Mathieu 2011 and Gosnell et al. 2019, albeit will less massive turnoffs).

WOCS 36011, on the other hand, has a shorter period of 217 d and a much higher eccentricity with $e \sim 0.74$. Blue stragglers with periods on the order of 10^2 days are likely the result of mass transfer from an RGB star, as in the case of WOCS 5379 in the open cluster NGC 188 (Gosnell et al. 2014; Mathieu & Geller 2015; Gosnell et al. 2019). Interestingly, the CMD location of WOCS 36011 in NGC 7789 relative to the ZAMS turnoff is very similar to that of WOCS 5379 in NGC 188 (although the primary star of WOCS 36011 is of higher mass).

Our analysis of the mass function of WOCS 36011 is inconclusive regarding the presence of a white dwarf companion from an RGB donor star, as we can only place a lower limit on the companion stellar mass of $\sim 0.05 M_{\odot}$. The very high eccentricity may be challenging to a mass-transfer origin modeling. This blue straggler, like its counterpart in NGC 188, is the subject of continued observation.

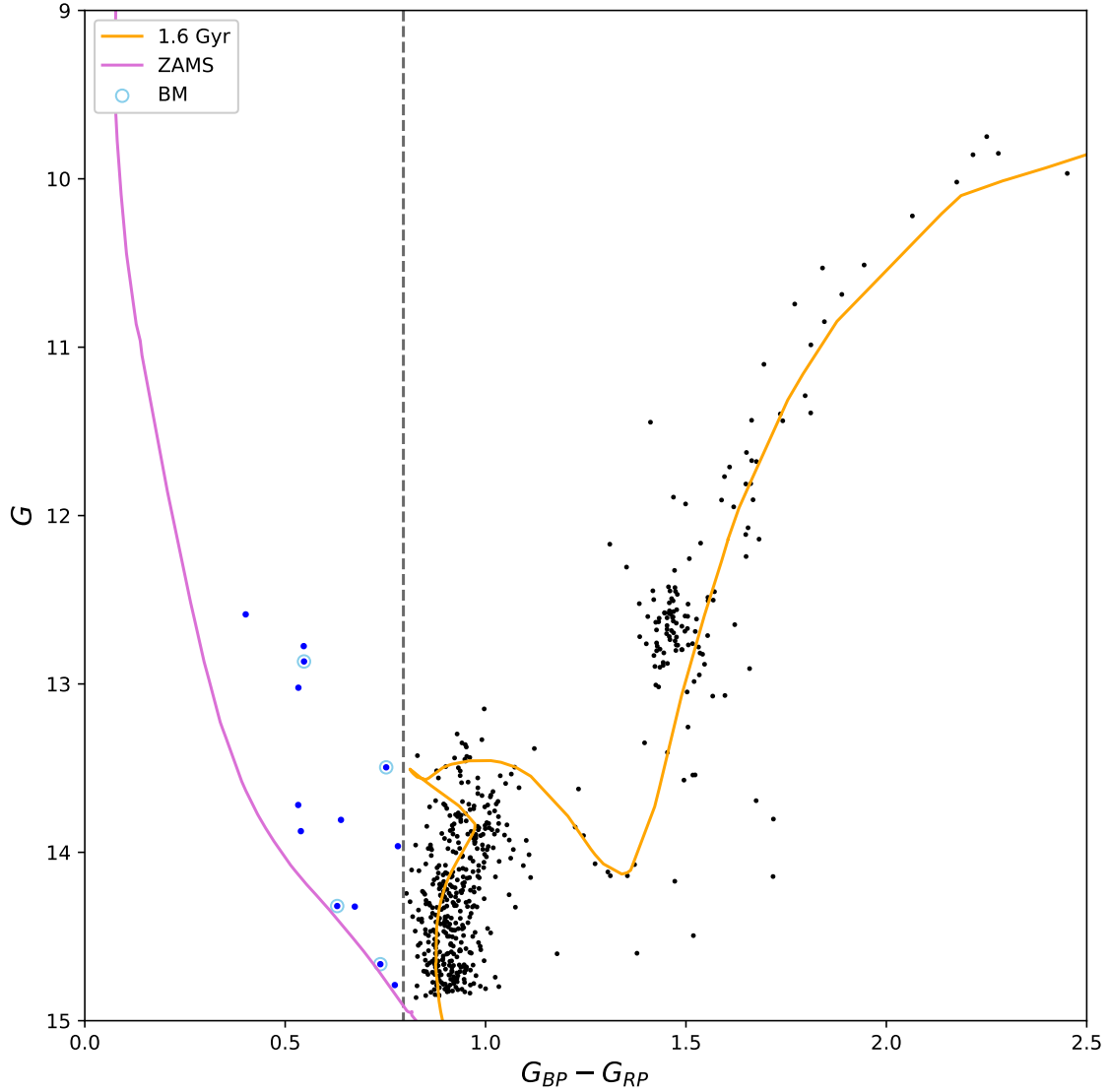


Figure 16. The *Gaia* DR2 CMD of NGC 7789 highlighting the BSS that fall to the blue of the dashed line. BSS non-velocity-variable RV members with $P_\mu \geq 50\%$ are indicated by blue dots. Binary BSS, all of which have orbital solutions, are marked with an additional circle. The curves are the same as in Figure 11.

WOCS 10011 has a similarly low period and significant eccentricity, with a period of 517 d and $e \sim 0.37$. It may be the case that this binary is not a true blue straggler, but rather on the cluster blue hook. For the purposes of this work, we consider it to be a blue straggler candidate and it remains the subject of continued study.

The long-period orbits we find for two of the NGC 7789 blue stragglers are in line with the BSS orbital periods found for the intermediate-aged open cluster NGC 6819 (2.5 Gyr) and the old open cluster NGC 188 (7 Gyr). For NGC 6819, the three SB1 BSS with orbital solutions have periods of 762 d, 1144 d, and 3900 d (Milliman et al. 2014). In NGC 188 all but one of the SB1 BSS (13/14) have a period on the order of 10^3 days (Geller & Mathieu 2012).

With the four detected velocity-variable BSS we find a BSS binary frequency of $31\% \pm 15\%$ (4/13). This is consistent with the $40\% \pm 16\%$ found for NGC 6819 (Milliman et al. 2014) and less than the $80\% \pm 20\%$ BSS binary fraction found for NGC 188 (Mathieu & Geller 2009) and the $79\% \pm 24\%$ BSS binary fraction found in M67 (Geller et al. 2015). If we exclude the borderline BSS candidates WOCS 10011, WOCS 25008, and WOCS 25024 the BSS binary frequency is then $30\% \pm 17\%$, still consistent with NGC 6819. Excluding also the other BSS candidate with high-noise astrometry, WOCS 4009, the binary frequency is then $33\% \pm 19\%$.

12. SUMMARY

We present the results of a complete and extensive time-series radial-velocity survey of 1206 stars in the open cluster NGC 7789. The stellar sample extends to a radius of $\sim 18'$ (10 pc in projection) from the cluster center and covers a G mag range from ~ 10 to 15. This magnitude range includes evolved MS stars to 1 mag below the turnoff, giants, red-clump stars, blue stragglers, and sub-subgiant candidates.

We use these radial-velocity measurements and *Gaia* DR2 data to derive a sample of 564 three-dimensional cluster members. We identify 105 velocity-variable cluster members, and present spectroscopic orbital solutions for 83 binaries. We calculate an incompleteness-corrected MS binary fraction of $31\% \pm 3\%$ for binaries with periods under 10,000 days, consistent with other open clusters studied by WOCS. We find a tidal circularization period of $8.22_{-1.35}^{+3.51}$ days, consistent with the ad hoc tidal dissipation rate of Geller et al. (2013).

We detect $31\% \pm 15\%$ of BSS as velocity variable, consistent with the frequency of velocity-variable BSS in the similarly-aged cluster NGC 6819. We also identify two BSS, WOCS 10011 and WOCS 36011, whose low periods and significant eccentricities may be the result of mass transfer from an RGB star.

We also find two sub-subgiants and two red stragglers in our sample. We note that the amplitude of the velocity variability of the sub-subgiant WOCS 20035 is lower than that of other sub-subgiants, which typically have short orbital periods. Neither of the red stragglers are velocity variables. We look forward to our expanded observations of NGC 7789 that will shed more light on these alternative stellar evolution products.

ACKNOWLEDGMENTS

The University of Wisconsin-Madison authors acknowledge funding support from NSF AST-1714506, the Graduate School, the Office of the Vice Chancellor for Research and Graduate Education at the University of Wisconsin-Madison, and the Wisconsin Alumni Research Foundation.

This work has made use of data from the European Space Agency (ESA) mission *Gaia* (<https://www.cosmos.esa.int/gaia>), processed by the *Gaia* Data Processing and Analysis Consortium (DPAC, <https://www.cosmos.esa.int/web/gaia/dpac/consortium>). Funding for the DPAC has been provided by national institutions, in particular the institutions participating in the *Gaia* Multilateral Agreement.

This work has also made use of Astropy (<http://www.astropy.org>), a community-developed core Python package for Astronomy (Astropy Collaboration et al. 2013, 2018), as well as MATLAB (MAT 2019).

This work was conducted at the University of Wisconsin-Madison which is located on occupied ancestral land of the Ho-chunk Nation, and observations for this work were conducted on the traditional lands of the Tohono O’odham Nation. We respect the inherent sovereignty of these nations, along with the other eleven First Nations in Wisconsin as well as the southwestern tribes of Arizona. We honor with gratitude these lands and the peoples who have stewarded them, and who continue to steward them, throughout the generations.

REFERENCES

- 2019, MATLAB version 9.6 (R2019a), The Mathworks, Inc., Natick, Massachusetts
- Astropy Collaboration, Robitaille, T. P., Tollerud, E. J., et al. 2013, *A&A*, 558, A33, doi: [10.1051/0004-6361/201322068](https://doi.org/10.1051/0004-6361/201322068)
- Astropy Collaboration, Price-Whelan, A. M., Sipócz, B. M., et al. 2018, *AJ*, 156, 123, doi: [10.3847/1538-3881/aabc4f](https://doi.org/10.3847/1538-3881/aabc4f)
- Barden, S. C., Armandroff, T., Muller, G., et al. 1994, in *Proc. SPIE*, Vol. 2198, *Instrumentation in Astronomy VIII*, ed. D. L. Crawford & E. R. Craine, 87–97
- Burbidge, E. M., & Sandage, A. 1958, *ApJ*, 128, 174, doi: [10.1086/146535](https://doi.org/10.1086/146535)
- Cantat-Gaudin, T., Jordi, C., Vallenari, A., et al. 2018, *A&A*, 618, A93, doi: [10.1051/0004-6361/201833476](https://doi.org/10.1051/0004-6361/201833476)
- Casamiquela, L., Carrera, R., Jordi, C., et al. 2016, *MNRAS*, 458, 3150, doi: [10.1093/mnras/stw518](https://doi.org/10.1093/mnras/stw518)
- Deliyannis, C. P., Anthony-Twarog, B. J., Lee-Brown, D. B., & Twarog, B. A. 2019, *AJ*, 158, 163, doi: [10.3847/1538-3881/ab3fad](https://doi.org/10.3847/1538-3881/ab3fad)
- Dotter, A. 2016, *ApJS*, 222, 8, doi: [10.3847/0067-0049/222/1/8](https://doi.org/10.3847/0067-0049/222/1/8)
- Fletcher, J. M., Harris, H. C., McClure, R. D., & Scarfe, C. D. 1982, *PASP*, 94, 1017, doi: [10.1086/131102](https://doi.org/10.1086/131102)
- Gaia Collaboration, Prusti, T., de Bruijne, J. H. J., et al. 2016, *A&A*, 595, A1, doi: [10.1051/0004-6361/201629272](https://doi.org/10.1051/0004-6361/201629272)
- Gaia Collaboration, Babusiaux, C., van Leeuwen, F., et al. 2018a, *A&A*, 616, A10, doi: [10.1051/0004-6361/201832843](https://doi.org/10.1051/0004-6361/201832843)
- Gaia Collaboration, Brown, A. G. A., Vallenari, A., et al. 2018b, *A&A*, 616, A1, doi: [10.1051/0004-6361/201833051](https://doi.org/10.1051/0004-6361/201833051)
- Gao, X.-h. 2018, *PASP*, 130, 124101, doi: [10.1088/1538-3873/aae0d2](https://doi.org/10.1088/1538-3873/aae0d2)

- Geller, A. M., Hurley, J. R., & Mathieu, R. D. 2013, *AJ*, 145, 8,
doi: [10.1088/0004-6256/145/1/8](https://doi.org/10.1088/0004-6256/145/1/8)
- Geller, A. M., Latham, D. W., & Mathieu, R. D. 2015, *AJ*, 150, 97,
doi: [10.1088/0004-6256/150/3/97](https://doi.org/10.1088/0004-6256/150/3/97)
- Geller, A. M., Leiner, E. M., Chatterjee, S., et al. 2017b, *ApJ*, 842, 1,
doi: [10.3847/1538-4357/aa72ef](https://doi.org/10.3847/1538-4357/aa72ef)
- Geller, A. M., & Mathieu, R. D. 2011, *Nature*, 478, 356,
doi: [10.1038/nature10512](https://doi.org/10.1038/nature10512)
- . 2012, *AJ*, 144, 54,
doi: [10.1088/0004-6256/144/2/54](https://doi.org/10.1088/0004-6256/144/2/54)
- Geller, A. M., Mathieu, R. D., Braden, E. K., et al. 2010, *AJ*, 139, 1383,
doi: [10.1088/0004-6256/139/4/1383](https://doi.org/10.1088/0004-6256/139/4/1383)
- Geller, A. M., Mathieu, R. D., Harris, H. C., & McClure, R. D. 2008, *AJ*, 135, 2264,
doi: [10.1088/0004-6256/135/6/2264](https://doi.org/10.1088/0004-6256/135/6/2264)
- Geller, A. M., Leiner, E. M., Bellini, A., et al. 2017a, *ApJ*, 840, 66,
doi: [10.3847/1538-4357/aa6af3](https://doi.org/10.3847/1538-4357/aa6af3)
- Gim, M., Hesser, J. E., McClure, R. D., & Stetson, P. B. 1998a, *PASP*, 110, 1172,
doi: [10.1086/316241](https://doi.org/10.1086/316241)
- Gim, M., Vandenberg, D. A., Stetson, P. B., Hesser, J. E., & Zurek, D. R. 1998b, *PASP*, 110, 1318,
doi: [10.1086/316266](https://doi.org/10.1086/316266)
- Gosnell, N. M., Leiner, E. M., Mathieu, R. D., et al. 2019, *ApJ*, 885, 45,
doi: [10.3847/1538-4357/ab4273](https://doi.org/10.3847/1538-4357/ab4273)
- Gosnell, N. M., Mathieu, R. D., Geller, A. M., et al. 2015, *ApJ*, 814, 163,
doi: [10.1088/0004-637X/814/2/163](https://doi.org/10.1088/0004-637X/814/2/163)
- . 2014, *ApJL*, 783, L8,
doi: [10.1088/2041-8205/783/1/L8](https://doi.org/10.1088/2041-8205/783/1/L8)
- Hurley, J. R., Tout, C. A., & Pols, O. R. 2002, *MNRAS*, 329, 897,
doi: [10.1046/j.1365-8711.2002.05038.x](https://doi.org/10.1046/j.1365-8711.2002.05038.x)
- Jacobson, H. R., Pilachowski, C. A., & Friel, E. D. 2011, *AJ*, 142, 59,
doi: [10.1088/0004-6256/142/2/59](https://doi.org/10.1088/0004-6256/142/2/59)
- Jahn, K., Kaluzny, J., & Rucinski, S. M. 1995, *A&A*, 295, 101
- Kroupa, P. 1995, *MNRAS*, 277, 1507
- Kurucz, R. L. 1993, in *Light Curve Modeling of Eclipsing Binary Stars*, ed. E. F. Milone (Springer-Verlag), 93–101
- Latham, D. W., Stefanik, R. P., & Carney, B. W. 1985, in *Stellar Radial Velocities*, ed. A. G. D. Philip & D. W. Latham, 381–384
- Leiner, E., Mathieu, R. D., & Geller, A. M. 2017, *ApJ*, 840, 67,
doi: [10.3847/1538-4357/aa6aff](https://doi.org/10.3847/1538-4357/aa6aff)
- Leiner, E., Mathieu, R. D., Vanderburg, A., Gosnell, N. M., & Smith, J. C. 2019, *ApJ*, 881, 47,
doi: [10.3847/1538-4357/ab2bf8](https://doi.org/10.3847/1538-4357/ab2bf8)
- Leiner, E. M., Mathieu, R. D., Gosnell, N. M., & Geller, A. M. 2015, *AJ*, 150, 10,
doi: [10.1088/0004-6256/150/1/10](https://doi.org/10.1088/0004-6256/150/1/10)
- Mathieu, R. D. 1983, *ApJL*, 267, L97,
doi: [10.1086/184011](https://doi.org/10.1086/184011)
- Mathieu, R. D. 2000, in *ASP Conf. Ser.*, Vol. 198, *Stellar Clusters and Associations: Convection, Rotation, and Dynamos*, ed. R. Pallavicini, G. Micela, & S. Sciortino, 517
- Mathieu, R. D., & Geller, A. M. 2009, *Nature*, 462, 1032,
doi: [10.1038/nature08568](https://doi.org/10.1038/nature08568)
- . 2015, in *Astrophysics and Space Science Library*, Vol. 413, *Ecology of Blue Straggler Stars*, ed. H. M. J. Boffin, G. Carraro, & G. Beccari (Springer-Verlag), 29–63
- Mathieu, R. D., & Leiner, E. M. 2019, in *The Impact of Binary Stars on Stellar Evolution*, Cambridge Astrophysics (Cambridge University Press), 261–276
- McNamara, B. J., & Solomon, S. 1981, *A&AS*, 43, 337
- Meibom, S., Barnes, S. A., Platais, I., et al. 2015, *Nature*, 517, 589,
doi: [10.1038/nature14118](https://doi.org/10.1038/nature14118)
- Meibom, S., Grundahl, F., Clausen, J. V., et al. 2009, *AJ*, 137, 5086,
doi: [10.1088/0004-6256/137/6/5086](https://doi.org/10.1088/0004-6256/137/6/5086)
- Meibom, S., & Mathieu, R. D. 2005, *ApJ*, 620, 970, doi: [10.1086/427082](https://doi.org/10.1086/427082)
- Milliman, K. E., Leiner, E., Mathieu, R. D., Tofflemire, B. M., & Platais, I. 2016, *AJ*, 151, 152,
doi: [10.3847/0004-6256/151/6/152](https://doi.org/10.3847/0004-6256/151/6/152)

- Milliman, K. E., Mathieu, R. D., Geller, A. M., et al. 2014, *AJ*, 148, 38, doi: [10.1088/0004-6256/148/2/38](https://doi.org/10.1088/0004-6256/148/2/38)
- Milliman, K. E., Mathieu, R. D., & Schuler, S. C. 2015, *AJ*, 150, 84, doi: [10.1088/0004-6256/150/3/84](https://doi.org/10.1088/0004-6256/150/3/84)
- Mochejska, B. J., & Kaluzny, J. 1999, *AcA*, 49, 351
- Overbeek, J. C., Friel, E. D., Jacobson, H. R., et al. 2015, *AJ*, 149, 15, doi: [10.1088/0004-6256/149/1/15](https://doi.org/10.1088/0004-6256/149/1/15)
- Paczyński, B. 1971, *ARA&A*, 9, 183, doi: [10.1146/annurev.aa.09.090171.001151](https://doi.org/10.1146/annurev.aa.09.090171.001151)
- Pancino, E., Carrera, R., Rossetti, E., & Gallart, C. 2010, *A&A*, 511, A56, doi: [10.1051/0004-6361/200912965](https://doi.org/10.1051/0004-6361/200912965)
- Platais, I., Gosnell, N. M., Meibom, S., et al. 2013, *AJ*, 146, 43, doi: [10.1088/0004-6256/146/2/43](https://doi.org/10.1088/0004-6256/146/2/43)
- Platais, I., Kozhurina-Platais, V., Mathieu, R. D., Girard, T. M., & van Altena, W. F. 2003, *AJ*, 126, 2922, doi: [10.1086/379677](https://doi.org/10.1086/379677)
- Raghavan, D., McAlister, H. A., Henry, T. J., et al. 2010, *ApJS*, 190, 1, doi: [10.1088/0067-0049/190/1/1](https://doi.org/10.1088/0067-0049/190/1/1)
- Rasio, F. A. 1995, *ApJL*, 444, L41, doi: [10.1086/187855](https://doi.org/10.1086/187855)
- Sandquist, E. L., Mathieu, R. D., Quinn, S. N., et al. 2018, *AJ*, 155, 152, doi: [10.3847/1538-3881/aab0ff](https://doi.org/10.3847/1538-3881/aab0ff)
- Sarajedini, A., von Hippel, T., Kozhurina-Platais, V., & Demarque, P. 1999, *AJ*, 118, 2894, doi: [10.1086/301149](https://doi.org/10.1086/301149)
- Taylor, M. B. 2005, in *Astronomical Society of the Pacific Conference Series*, Vol. 347, *Astronomical Data Analysis Software and Systems XIV*, ed. P. Shopbell, M. Britton, & R. Ebert, 29
- Thompson, B., Frinchaboy, P., Kinemuchi, K., Sarajedini, A., & Cohen, R. 2014, *AJ*, 148, 85, doi: [10.1088/0004-6256/148/5/85](https://doi.org/10.1088/0004-6256/148/5/85)
- Tofflemire, B. M., Gosnell, N. M., Mathieu, R. D., & Platais, I. 2014, *AJ*, 148, 61, doi: [10.1088/0004-6256/148/4/61](https://doi.org/10.1088/0004-6256/148/4/61)
- van Dokkum, P. G. 2001, *PASP*, 113, 1420, doi: [10.1086/323894](https://doi.org/10.1086/323894)
- Webbink, R. F. 1976, *ApJ*, 209, 829, doi: [10.1086/154781](https://doi.org/10.1086/154781)
- Wu, Z.-Y., Du, C.-H., Ma, J., & Zhou, X. 2009, *Chinese Physics Letters*, 26, 029701, doi: [10.1088/0256-307X/26/2/029701](https://doi.org/10.1088/0256-307X/26/2/029701)
- Wu, Z.-Y., Zhou, X., Ma, J., et al. 2007, *AJ*, 133, 2061, doi: [10.1086/512189](https://doi.org/10.1086/512189)
- Yang, S.-C., Sarajedini, A., Deliyannis, C. P., et al. 2013, *ApJ*, 762, 3, doi: [10.1088/0004-637X/762/1/3](https://doi.org/10.1088/0004-637X/762/1/3)
- Zahn, J.-P., & Bouchet, L. 1989, *A&A*, 223, 112
- Zhang, X.-B., Deng, L.-C., Xin, Y., & Zhou, X. 2003, *ChJA&A*, 3, 151
- Zucker, S., & Mazeh, T. 1994, *ApJ*, 420, 806, doi: [10.1086/173605](https://doi.org/10.1086/173605)